Applied Energy 367 (2024) 123327

Contents lists available at ScienceDirect

Applied Energy

journal homepage: www.elsevier.com/locate/apenergy

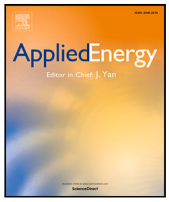

A coupled electrothermal lithium-ion battery reduced-order model including heat generation due to solid diffusion

Pablo Rodríguez-Iturriaga [a], Víctor Manuel García [c], Salvador Rodríguez-Bolívar [a,*], Enrique Ernesto Valdés [b], David Anseán [b], Juan Antonio López-Villanueva [a]

[a] Department of Electronics and Computer Technology, Faculty of Sciences, University of Granada, Granada, 18071, Andalusia, Spain
[b] Department of Electrical Engineering, Polytechnic School of Engineering, University of Oviedo, Gijon, 33204, Asturias, Spain
[c] Department of Physical and Analytical Chemistry, Polytechnic School of Engineering, University of Oviedo, Gijon, 33204, Asturias, Spain

ARTICLE INFO

Keywords:
Lithium-ion battery
Physics-based ECM
Electrothermal modeling
Heat generation
EIS-aided parameterization

ABSTRACT

Temperature constitutes a critical variable in the operation of lithium-ion batteries, given its major influence on their behavior, as well as for safety reasons in real-world applications. Therefore, it is imperative to develop accurate thermal models along with precise cell characterizations at different ambient temperatures. These two aspects are often analyzed independently; however, a coupled modeling approach is required in order to replicate cell behavior in a broad range of operating scenarios due to non-negligible self-heating. In this article, we present a coupled electrothermal reduced-order model which is able to yield highly accurate results upon validation against experimental data, both in output voltage (≤ 25 mV RMS) and cell temperature (≤ 0.68°C RMS) at a low computational cost with a unique set of 7 well-defined parameters, in the range from 50 °C to 0 °C ambient temperatures. A key idea is the consideration of the contributions of entropic heat and solid diffusion to overall heat generation, which proves to be necessary so as to qualitatively and quantitatively explain the evolution of cell temperature throughout a full discharge. The proposed model provides an excellent trade-off between accuracy and computational and parameterization complexities in a wide interval of operating conditions, therefore being suitable alternative for its implementation in practical applications.

1. Introduction

The demand for energy storage solutions has steadily increased in recent years, driven by the spread of renewable energy systems [1,2] and electric vehicles. Lithium-ion batteries (LIBs) are regarded as a key enabling storage technology due to their high performance, prolonged cycle life and low self-discharge [3]. Given the significant influence that temperature has on battery behavior [4–6], thermal modeling and management proves to be a critical aspect for accurate predictions of their performance by a Battery Management System (BMS) [7,8], while ensuring a safe operating window and preventing issues such as thermal runaway by a Battery Thermal Management System (BTMS) [9–11]. Consequently, the development of electrothermal models, in which both electrical and thermal aspects are integrated, plays a pivotal role in achieving the former goals. For this purpose, the analysis of three main aspects emerges: thermal dependencies of model parameters, computation of heat generation, and thermal modeling. Although these aspects may be addressed separately, they are closely interrelated: parameter values determine cell heat generation, which is the input to an appropriate thermal model that outputs the temperature increase with respect to ambient temperature. This is required so as to update the values of model parameters according to their thermal dependency, which subsequently impacts heat generation. For this reason, electrical and thermal aspects of battery behavior are coupled, and must be treated in a way that accounts for the feedback between both, with the goal of reproducing battery operation accurately and developing more robust and efficient BMSs.

Temperature is known to be a critical factor in parameters for both electrochemical and equivalent circuit battery models (ECMs). In electrochemical models, diffusion coefficients and reaction rates are usually assumed to vary with temperature according to respective Arrhenius relationships [12]. Nevertheless, parameterization constitutes the main challenge [13,14] within this modeling framework, since the values of over 30 physical parameters are required [15,16], which cannot be uniquely determined from current–voltage data and necessitate destructive electrochemical evaluations following cell disassembly and

* Corresponding author.
E-mail address: rbolivar@ugr.es (S. Rodríguez-Bolívar).

https://doi.org/10.1016/j.apenergy.2024.123327
Received 6 February 2024; Received in revised form 29 March 2024; Accepted 27 April 2024
Available online 9 May 2024

tear-down [17]. For this reason, identifying temperature dependencies in physical parameters becomes increasingly complex [18,19].

Conversely, there is usually not a clear translation between electrochemical models and ECMs, so the relationship between physical and circuit parameters is typically lost for the latter approach, and the subsequent electrical parameters may not contain a clear physical meaning. Furthermore, there is not a unique and well-defined parameterization methodology for standard ECMs [20]; therefore, a rigorous thermal characterization of circuit parameters is not often possible as a result. In this regard, some authors have suggested polynomial expressions for the temperature dependency of resistors and capacitors [21,22]; however, this thermal characterization is not general and depends on the procedure by which the values of circuit parameters themselves have been determined. For this reason, circuit parameters are often treated adaptively so as to factor in these variations [21,23–26], and used in conjunction with Kalman filters for the joint estimation of state of charge (SOC) and cell temperature [22,25,27–29]. The aforementioned approach may be improved by the development of reduced-order models in which there is a direct correlation between physical and circuit states [30]. In these models, physical parameters are grouped into circuit parameters for a simpler parameterization [31]. Proceeding in this manner, a more general thermal characterization of circuit parameters may be performed in a way that bears a closer resemblance to that of electrochemical models.

Regarding the calculation of the heat generation rate, an energy balance for battery systems was carried out in the pioneering work by Bernardi et al. [32], whose general expressions have been subsequently incorporated or adapted into electrical and electrochemical models with varying degrees of complexity. If a standard multiple-RC equivalent circuit model is considered, heat generation simplifies to the addition of the product of cell current and overpotential and the entropic term, as in $P = (V - OCV)I + IT\frac{\partial OCV}{\partial T}$ [33,34], where OCV is the Open Circuit Voltage evaluated at the current SOC, V and T are cell voltage and temperature, and I is cell current, considered positive while charging. The first term is commonly understood as Joule heating since it can be expressed in the form $R_{eq}I^2$, whereas the entropic or reversible term $IT\frac{\partial OCV}{\partial T}$ presents a dependency on I instead of I^2, and is sometimes neglected at high current rates as a result [16]. However, simplified ECMs establish a clear separation between thermodynamic behavior, represented in the relationship between OCV and SOC [35], from dynamic behavior, described by parallel RC networks connected in series with the OCV source. In consequence, the equilibrium potential is evaluated at the current SOC or average lithium concentration in active material particles instead of the surface concentration [31,36,37], therefore calculating solid potential in a different manner from electrochemical models [15]. Given that this distinction between surface and average concentrations is not made in standard ECMs [38], the effect of solid diffusion in the electrode particles is assumed to be modeled by the parallel RC networks. For this reason, within this modeling framework, solid diffusion is implicitly assumed to make a significant contribution to heat generation, which cannot be treated separately from pure Joule heating.

In the case of electrochemical approaches, some authors have discussed the possibility of including additional terms that contribute to the overall heat generation, such as the term known as heat of mixing [39,40]. This term is ascribed to the non-homogeneous distribution of active chemical species within the spatial structure of the battery cell and may be experimentally measured during relaxation periods [41]. Nevertheless, there is not an unambiguous mathematical definition and interpretation of heat of mixing, either a conclusive consensus on its quantitative significance in comparison to other sources of heat generation [40–42]. In consequence, some electrochemical approaches consider that the solid diffusion process does not affect heat generation [16] and only Joule heating terms due to electrolyte, charge transfer and ohmic losses are taken into account. However, this would cause a substantial discrepancy in the magnitude of the heat generation rate in comparison to standard ECMs, as the difference between surface and average concentrations of lithium within the active particles may entail a significant overpotential that is implied in the latter modeling approach. For this reason, a different expression is required for the calculation of heat generation that factors this aspect in when a physics-based approach is employed.

Some of the aforementioned issues for an accurate calculation of heat generation may be alleviated by the use of physics-based ECMs [36,43,44], whose topology and structure have a direct correlation to electrochemical models. In consequence, they are able to provide information about electrochemical states at a lower computational cost and may also be parameterized more easily from non-destructive experimental tests [45]. As stated previously, a circuit model that allows for the computation of both surface and average lithium concentrations within active material particles, is required in order to compute solid potential in a similar manner to electrochemical models [36,37]. In a previous article [31], we analytically derived a reduced-order model from the enhanced Single Particle Model (SPMe), and the resulting ECM was composed of two separate sections for solid diffusion and macroscale electrical behavior, respectively. This model was subsequently extended in [46] in order to account for spatial electrode structure [47–49] and a distribution of particle sizes [50]. Both models allowed for a simpler parameterization process from experimental Electrochemical Impedance Spectroscopy (EIS) data, and the latter was able to explain experimentally observed complex behavior in a wide interval of current rates and ambient temperatures due to its discretely distributed topology. Nevertheless, a considerable self-heating effect was observed, which impacted model accuracy in output voltage, especially at high current rates and low ambient temperatures, as has also recently been noted in [19]. Therefore, we concluded that instantaneous cell temperature should be incorporated into models in a coupled manner, which motivates a rigorous thermal characterization of electrical parameters and a careful analysis of contributions to heat generation that are not commonly considered in standard ECMs [51].

For the reasons above, in this article we present a coupled electrothermal model based on the discretely distributed topology, in which electrical parameters are updated continuously as a function of the temperature estimated via a thermal model including the contribution of solid diffusion to heat generation. The final model is dependent on three electrical parameters (R_{ohm}, R_{ct} and τ_d), two activation energies E_a, for charge transfer and the solid diffusion processes, respectively, and two parameters, R_{th} and τ_{th}, for the thermal model, with which to simulate the behavior of the cell in any operating scenario. Additionally, the direct translation of the model into the frequency domain allows for a unique and well-defined parameterization process using experimental EIS data. Model results are qualitatively and quantitatively analogous to experimental data with a low computational cost, which make it a suitable alternative for its implementation in BMSs.

The main contributions of the present article are summarized below:

1. Characterizing the temperature dependency of the electrical parameters of a discretely distributed, physics-based ECM by taking advantage of its associated frequency response.
2. Proposing a novel expression for the heat generation rate based on said electrical model including the contribution of solid diffusion.
3. Integrating the electrical model and the thermal model in a complete coupled electrothermal model, which is valid for a wide range of current rates and ambient temperatures.

Consequently, the present article is structured in the following Sections: the proposed modeling approach, including electrical and thermal aspects, is detailed in Section 2, whereas the experimental testing is described in Section 3. The parameterization process as well as the experimental validation are thoroughly discussed in Section 4, and some final remarks are presented in the last Section.

2. Model development

In this Section, the discretely distributed equivalent circuit model is presented, and a novel expression for heat generation is derived including the effect of solid diffusion.

2.1. Equivalent circuit model

In our previous article [46], a distributed, multi-particle ECM was developed with the purpose of explaining complex behavior in the interval of moderate to high current rates. Said model considered a particle size distribution so as to account for experimentally observed electrode heterogeneity, as well as a distribution in the spatial dimension in order to bear a resemblance to the electrode structure defined in the Doyle–Fuller–Newman (DFN) model. However, a key difference with most DFN implementations lies in the fact that the model is discretely distributed and not continuously, via a macroscopic ohmic resistance R_{ohm}. This is due to the fact that particle size cannot be considered microscopic in relation to electrode thickness, as is apparent from different parameter sets for electrochemical models [15–17]. It was also observed that the proposed circuit topology had a greater impact on cell voltage than a distribution of particle sizes during constant-current operation. As the focus of this article is on thermal behavior, which is more clearly visible in this operating regime, only one particle size will be considered in this case at each circuit node. The presence of a distribution of particle sizes is presumed to influence relaxation profiles more heavily [52], so we leave open the possibility of including it in future works where this aspect of battery behavior is characterized more thoroughly.

The electrical model considered in this article, shown in Fig. 1-(a), consists of 4 identical active material particles, whose circuit equivalent is the series connection of a dependent voltage source $OCV(\chi_s)$ and the charge transfer resistance R_{ct}. Active material particles are connected to their neighbors by the ohmic impedance R_{ohm} associated to conductive losses in the solid and the electrolyte, in such a way that particle behavior depends only on their position along the electrode. A relevant feature of this model is the distinction between surface and average concentrations within each particle, χ_s and $\overline{\chi}$, by means of auxiliary subcircuits shown in Fig. 1-(b) that model the solid diffusion process accurately. Therefore, the equilibrium potential OCV may be evaluated at the surface concentration in each particle χ_s, thus bearing a closer resemblance to how the solid potential is computed in electrochemical models.

Effective parameters are assumed for both electrodes in order to simplify the parameterization process [31,37], so only one main circuit branch is defined and the full-cell OCV is employed instead of electrode Open Circuit Potentials (OCPs). In consequence, if cell capacity Q_{cell} and full-cell OCV are known, the model only depends on 3 parameters: R_{ohm}, R_{ct}, and τ_d, which is the time constant related to the solid diffusion process. The discretely distributed circuit topology may also be maintained, although circuit nodes can no longer be assigned to specific electrode positions. The proposed ECM may be mirrored in order to account for both electrodes separately, resulting in a more challenging parameterization from full-cell data nonetheless.

Charge transfer overpotentials are linearized to constant charge transfer resistances in this work [15,31], according to Eq. (1):

$$R_{ct}(I) = \frac{2RT}{FI_0}\left[\frac{I_0}{I}\sinh^{-1}\left(\frac{I}{I_0}\right)\right] \rightarrow R_{ct} \approx \frac{2RT}{FI_0} \tag{1}$$

where I_0 is the exchange current. This linearization is accurate when $I < I_0$, which depends on temperature and SOC. Nevertheless, it will be considered valid in all cases so that the resulting model does not contain transcendental equations, and thus, may be analytically solved at every timestep. Given that no particle size distribution has been considered in this article, an approximation based on the distribution of 3 time constants, as defined in Eq. (2), is regarded as sufficiently accurate for the impedance Z_{DIFF}, related to the solid diffusion process after subtracting integration dynamics.

$$Z_{DIFF}(s) = \frac{K_d}{\sqrt{\tau_d s}\coth\left(\sqrt{\tau_d s}\right) - 1} - \frac{3K_d}{\tau_d s} \approx \frac{K_d}{5}\left(\frac{a_1}{1+b_1\tau_d s} + \frac{a_2}{1+b_2\tau_d s} + \frac{a_3}{1+b_3\tau_d s}\right) \tag{2}$$

where coefficient values a_i, b_i are shown in Table 1 and have been determined according to the distribution of relaxation times (DRT) associated with $Z_{DIFF}(s)$ [53]. This approximation, in addition to being computationally efficient, allows for a direct calculation of the state-space representation at every timestep when the time constant τ_d is updated dynamically as a function of cell temperature.

Table 1
Coefficient values for the approximation in Eq. (2).

i	1	2	3
a_i	0.5344	0.2724	0.1932
b_i	0.0479	0.0101	0.0020

The proposed ECM is able to provide extended physical insight with respect to standard ECMs, since it contains an accurate approximation of the solid diffusion process and accounts for the spatial distribution which is a defining trait of the DFN model. Conversely, an advantageous feature with regard to electrochemical models lies in parameterization: the model is completely defined by 3 electrical parameters, namely R_{ohm}, R_{ct} and τ_d, as parameters K_d and τ_d in Eq. (2) are correlated by the integrator constant: $Q = \frac{\tau_d}{3K_d}$, which stands for particle capacity. Therefore, the approach presented in [46] produced a model which could be parameterized in a simpler, more direct fashion, and was able to provide qualitatively and quantitatively accurate results upon validation against experimental data. However, the model progressively lost accuracy with decreasing ambient temperature, which suggests that thermal behavior and its effects on electrical parameters must be incorporated into the model in a coupled manner.

2.2. Thermal modeling

As discussed in the Introduction, both reaction rates and diffusion coefficients are assumed to change with temperature according to an Arrhenius equation, with the activation energy E_a being left as the fitting parameter in each case. One advantage of the proposed ECM is the clear correlation between physical and electrical processes, in such a way that the Arrhenius dependency may be maintained instead of other empirical or polynomial relationships [21,22], which may also be characterized from the frequency response of the battery cell. Once the thermal dependency of electrical parameters has been determined, the fully characterized electrical model has to be coupled with a thermal model with the goal of calculating self-heating induced by operation and update electrical parameters continuously as a function of the estimated cell temperature.

In this article, we take the heat generation equation proposed by Bernardi et al. [32] in Eq. (3) as a starting point:

$$P_{gen} = I(V_{cell} - U_{avg}) + IT\frac{\partial U_{avg}}{\partial T} \tag{3}$$

where P_{gen} is the heat generation rate, V_{cell} is cell terminal voltage, U_{avg} is the equilibrium potential, T is cell temperature, $\frac{\partial U_{avg}}{\partial T}$ is the entropic coefficient, and I is the applied current, considered positive while charging. Within the framework of the SPMe, cell output voltage may be broken down into the addition of its components as in Eq. (4) [15,31]:

$$V_{cell} = U_{sup} + \eta_{ct} + \eta_{ce} + \Delta\Phi_{ohm} \tag{4}$$

where U_{sup} is the equilibrium potential evaluated at the surface concentration of active material particles, η_{ct} is the charge transfer reaction

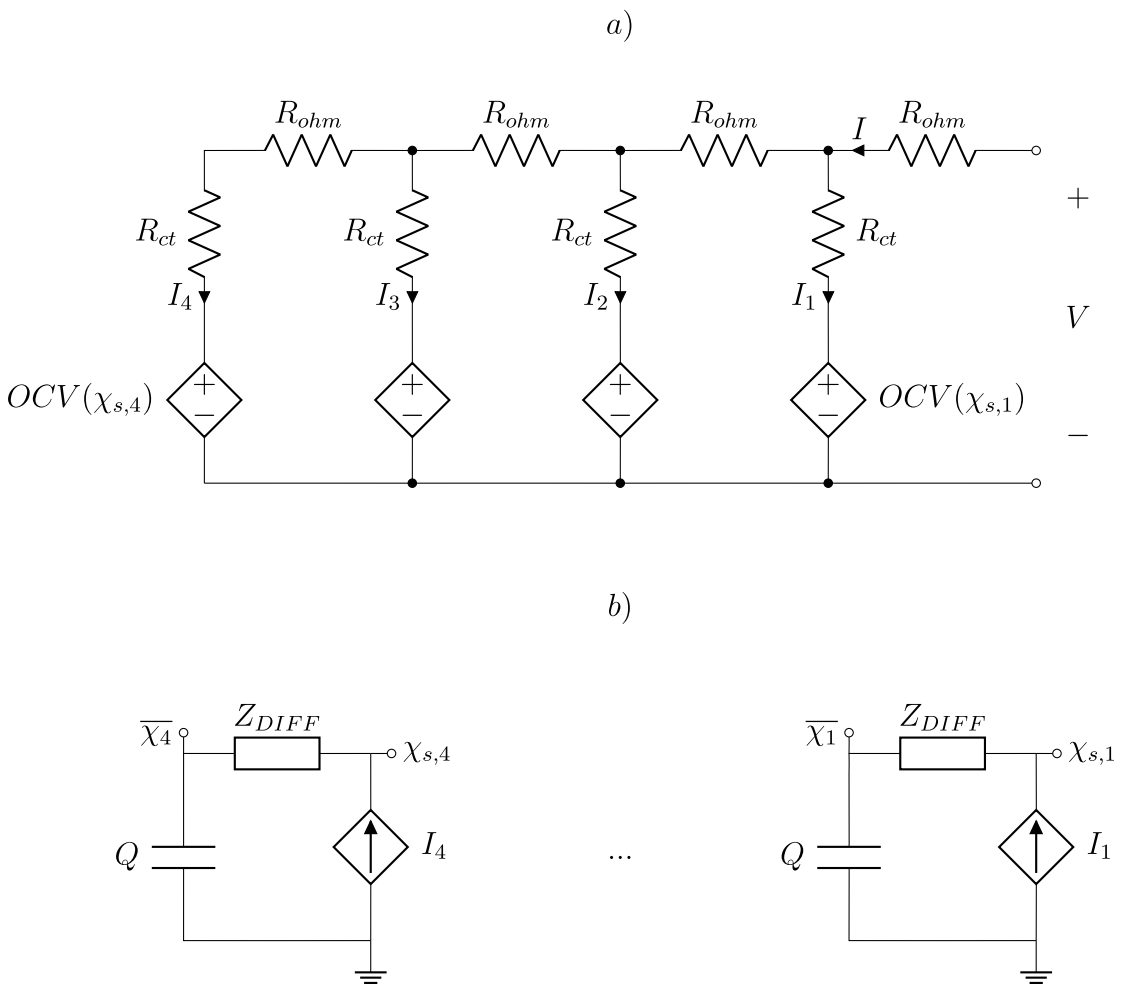

Fig. 1. Discretely distributed ECM. Circuit (a) accounts for macroscale behavior, while auxiliary subcircuits in (b) model the solid diffusion process in active material particles. Z_{DIFF} symbolizes the impedance corresponding to solid diffusion after subtracting integration dynamics, while Q indicates the capacity corresponding to each particle.

overpotential, η_{ce} is the overpotential due to concentration gradients in the electrolyte, and $\Delta\Phi_{ohm}$ is the voltage drop caused by ohmic losses in the solid and electrolyte. Substituting the expression for V_{cell} into Eq. (3) yields Eq. (5):

$$P_{gen} = I(U_{sup} - U_{avg}) + I\eta_{ct} + I\eta_{ce} + I\Delta\Phi_{ohm} + IT\frac{\partial U_{avg}}{\partial T} \tag{5}$$

If overpotentials are linearized, the previous expression may be simplified to that in Eq. (6):

$$P_{gen} = I(U_{sup} - U_{avg}) + I^2R_{ct} + I^2R_{ce} + I^2R_{ohm} + IT\frac{\partial U_{avg}}{\partial T} \tag{6}$$

where R_{ct} is the charge transfer resistance, R_{ce} is the resistance associated with concentration gradients in the electrolyte and R_{ohm} is the ohmic resistance. One may notice that the term $I(U_{sup} - U_{avg})$ arises in addition to Joule heating terms and the reversible heating term $IT\frac{\partial U_{avg}}{\partial T}$. It is noted that Eq. (3) from [32] was derived as a general energy balance for battery systems, and not specifically for intercalation systems; therefore the term U_{avg} is not precisely defined. The proposed ECM in Fig. 1 allows computing average and surface concentrations separately in each active material particle. Therefore, when applying the energy balance in Eq. (3) to Li-ion batteries, one may approximate U_{sup} by $OCV(\chi_s)$ and U_{avg} by $OCV(\overline{\chi})$. We can introduce η_{diff} as the diffusion overpotential [54], defined in Eq. (7):

$$\eta_{diff} = OCV(\chi_s) - OCV(\overline{\chi}) \tag{7}$$

The term $I\eta_{diff}$ may be interpreted as the heat generation due to the solid diffusion process [44,51], and it is noted that is both irreversible and exothermic in constant-current operation [40], since $I > 0$ and $U_{sup} > U_{avg}$ while charging and vice versa while discharging. Regarding dynamic operating conditions, one may notice that current fluctuations are usually several orders of magnitude faster than solid diffusion timescales. In consequence, quick changes in current are heavily attenuated by the solid diffusion process, resulting in small variations in concentration. Therefore, the solid diffusion overpotential $\eta_{diff} = OCV(\chi_s) - OCV(\overline{\chi})$ is close to zero as $\chi_s \approx \overline{\chi}$, and its contribution to the overall heat generation is negligible in comparison that of ohmic losses. Conversely, its influence may be significant in relaxation periods due to the prolonged inertia of the solid diffusion process. However, calculating heat generation in such circumstances requires accurate modeling of voltage relaxation profiles, which is outside the scope of this work and will be considered in future research.

As a result of Eq. (6), the contribution of solid diffusion to heat generation is accounted for in a way that implicitly considers the shape of the OCV-SOC curve, which has also been suggested recently in [55] but attributed to hysteresis voltage instead of the diffusion overpotential defined in Eq. (7). The magnitude of this term is not negligible in regions where the OCV-SOC curve exhibits a large slope, and also at high current rates that produce considerable concentration gradients in active material particles. Failing to take this term into account may result in inaccurate estimations of both heat generation and cell temperature [51], which highlights the importance of employing physics-based reduced-order models in which both the surface and average concentrations are well-defined model states [31,36,37]. In the case of a model that considers the spatial distribution across

the electrode, such as the DFN model, the heat generation rate can be calculated at every point of the x dimension by substituting local currents and concentrations in Eq. (6), and then added up along the spatial structure, so as to incorporate the local contributions of solid diffusion as suggested in [56].

For all the reasons above, and as a consequence of the circuit topology in Fig. 1, the different contributions to heat generation may be computed according to Eq. (8), where $U = OCV$ and R_{ce} has been lumped together with R_{ohm}. In this article, the entropic term is considered to be caused by the intercalation reaction and not the exchange reaction, so the derivative $\frac{\partial OCV}{\partial T}$ will be evaluated at the average concentration in each particle [32].

$$P_{cell} = P_{ohm} + P_{ct} + P_{diff} + P_{ent} \tag{8a}$$

$$P_{ohm} = R_{ohm}\left[I_4^2 + (I_4+I_3)^2 + (I_4+I_3+I_2)^2 + (I_4+I_3+I_2+I_1)^2\right] \tag{8b}$$

$$P_{ct} = R_{ct}\left[I_4^2 + I_3^2 + I_2^2 + I_1^2\right] \tag{8c}$$

$$P_{diff} = I_4\eta_{diff,4} + I_3\eta_{diff,3} + I_2\eta_{diff,2} + I_1\eta_{diff,1} \tag{8d}$$

$$P_{ent} = T\left[I_4\frac{\partial OCV}{\partial T}\bigg|_{\overline{\chi}_4} + I_3\frac{\partial OCV}{\partial T}\bigg|_{\overline{\chi}_3} + I_2\frac{\partial OCV}{\partial T}\bigg|_{\overline{\chi}_2} + I_1\frac{\partial OCV}{\partial T}\bigg|_{\overline{\chi}_1}\right] \tag{8e}$$

where $I_{1,2,3,4}$ are the currents through each particle as defined in Fig. 1. We would like to point out the convenience of the proposed circuit topology in Fig. 1, in the sense that both the surface and average concentrations of each particle are accessible model states, and the heat generation due to solid diffusion can be computed for each particle directly from the reduced-order equivalent circuit model as a result. It is noted that, due to the employed circuit topology, the heating term associated with ohmic losses will be the largest throughout most of a constant-current discharge, except for the regions where the gradient of the OCV vs. SOC curve is large. The influence of the entropic term will be most noticeable at lower current rates, especially in the SOC regions where it is endothermic. In any case, we consider that taking all four terms into account is necessary for an accurate description of cell thermal behavior, as will be discussed in Section 4.2.

Finally, the calculated heat generation rate is treated as the input of a lumped thermal model [57] considering homogeneous cell temperature [41] and forced convection towards the environment [58], where the state variable ΔT is the difference between cell and ambient temperatures. This thermal model only requires two parameters: a thermal resistance R_{th} and a thermal time constant τ_{th}, and its ordinary differential equation is shown below:

$$\tau_{th}\frac{d(\Delta T)}{dt} + \Delta T = R_{th}P_{cell} \tag{9}$$

We understand that a more elaborate thermal model could be developed and implemented; however, a lumped thermal model is consistent with literature for cylindrical 18 650-format cells [16,59–62]. Furthermore, there is not a clear correlation between the spatial dimension of the electrical model and the macroscale radial dimension of the cylindrical cell if a temperature gradient within the cell were to be considered [41]. Therefore, a lumped thermal model considering homogeneous cell temperature is the most suitable in this case, since the proposed electrothermal model will be validated against experimental data including surface temperature measurements. The thermal model could be extended to include an estimation of internal temperature [26]; nevertheless, we believe that the heat generation rate has a stronger influence on the observed complexity in cell thermal behavior than the thermal model itself. It is also possible to include ambient temperature as a dynamical input to the thermal model. However, it has been shown that ambient temperature acts as a direct term if its variations are slower than the thermal time constant τ_{th} [63], which is the case in most practical applications. This implies that a slowly changing ambient temperature instead of a constant value can be safely added up to the computed temperature increase to calculate cell temperature [26]. A more sophisticated modeling approach would be required in a situation where ambient temperature varies significantly as well as rapidly in comparison to cell dynamic behavior.

2.3. Model implementation

In this Section, a brief overview of the simulation flow is sketched, so as to clarify the implementation of both the electrical and thermal submodels, as well as the coupling between them. The simulation of the coupled model can be synthesized in four steps, which are performed sequentially at every timestep:

1. **Updating of temperature-dependent parameters.** Based on an Arrhenius relationship, parameters I_0 for charge transfer and τ_d for solid diffusion are updated as a function of the cell temperature calculated in the previous timestep, according to Eq. (10):

$$I_0 = A_{ct}\exp\left(-\frac{E_{a,ct}}{RT}\right), \qquad \tau_d = A_d\exp\left(\frac{E_{a,d}}{RT}\right) \tag{10}$$

The updated charge transfer resistance can be directly computed as $R_{ct} = \frac{2RT}{FI_0}$.

2. **Updating of state-space matrices and solid diffusion states.** Based on the approximation in Eq. (2), the coefficient values in Table 1, and the updated value of the solid diffusion time constant τ_d, the state-space matrices are calculated as follows:

$$A = diag\left[1 \quad \exp\left(-\tfrac{\Delta t}{b_1\tau_d}\right) \quad \exp\left(-\tfrac{\Delta t}{b_2\tau_d}\right) \quad \exp\left(-\tfrac{\Delta t}{b_3\tau_d}\right)\right] \tag{11a}$$

$$B = \left[-\tfrac{\Delta t}{Q_p} \quad 1-\exp\left(-\tfrac{\Delta t}{b_1\tau_d}\right) \quad 1-\exp\left(-\tfrac{\Delta t}{b_2\tau_d}\right) \quad 1-\exp\left(-\tfrac{\Delta t}{b_3\tau_d}\right)\right]^T \tag{11b}$$

$$C = \frac{K_d}{5}\begin{bmatrix}1 & a_1 & a_2 & a_3\end{bmatrix} \tag{11c}$$

where Q_p is the capacity of each particle, and $K_d = \frac{\tau_d}{3Q_p}$. Next, the states for solid diffusion for each particle are updated with their input being their respective current calculated in the previous timestep. The outputs of these systems are computed, which correspond to the surface concentration of each particle $\chi_{s,n}$.

3. **Calculation of the current distribution.** The current distribution can be calculated as the solution to the linear system of equations in Eq. (12), where $OCV_n = OCV(\chi_{s,n})$ and I_{cell} is the cell input current for the present timestep.

$$\begin{bmatrix} R_{ohm}+R_{ct} & -R_{ct} & 0 & 0 \\ R_{ohm} & R_{ohm}+R_{ct} & -R_{ct} & 0 \\ R_{ohm} & R_{ohm} & R_{ohm}+R_{ct} & -R_{ct} \\ 1 & 1 & 1 & 1 \end{bmatrix}\begin{bmatrix} I_4 \\ I_3 \\ I_2 \\ I_1 \end{bmatrix} = \begin{bmatrix} OCV_3 - OCV_4 \\ OCV_2 - OCV_3 \\ OCV_1 - OCV_2 \\ I_{cell} \end{bmatrix} \tag{12}$$

In this particular case, a manageable analytical solution to the system may be obtained, which proves more computationally efficient than solving the system numerically. The computed currents will be the input to the state-space approximation to the solid diffusion process for the next timestep. Once the current distribution has been determined, the calculation of cell terminal voltage follows immediately.

4. **Calculation of heat generation and cell temperature.** Once the parameters and states of the electrical model have been updated, heat generation is computed according to Eq. (8). The calculated heat generation is the input to the thermal model in Eq. (9), whose state-space representation is:

$$A = \exp\left(-\frac{\Delta t}{\tau_{th}}\right) \qquad B = R_{th}\left(1-\exp\left(-\frac{\Delta t}{\tau_{th}}\right)\right) \tag{13}$$

Once the temperature increase has been updated, cell temperature is computed by simply adding up ambient temperature.

It is noted that solid diffusion lags the current distribution by one timestep, in the same way that the electrical model lags the thermal model. Nevertheless, if the timestep is selected to be sufficiently smaller than the solid diffusion and thermal time constants, which is usually the case in practical applications, the coupling between processes is effective. A sequential implementation with a shorter timestep proves more computationally efficient than a numerical simultaneous solution for all the coupled processes.

3. Experimental

The experiments were conducted on six Samsung-SDI (INR18650-25R) cylindrical NMC/Gr cells from the same batch, whose nominal capacity, specified by the manufacturer, is 2500 mAh at their nominal C/5 discharge rate within operating voltage window ranging from 2.5 V to 4.2 V. The negative electrode was made of standard graphite, while the positive electrode resembled NMC-811, based on ex-situ surface science analysis [64]. The number of cells was chosen to ensure that cell-to-cell variation remained within acceptable limits, preventing the inclusion of outliers. The batch's comparability was established and validated in a prior work [46], resulting in a capacity retention of 2490.2 ± 0.4134% mAh and a delivered energy of 9.2064 ± 0.4134% Wh, when evaluated under the manufacturer's recommended testing guidelines.

The experimental designs were divided into three sequential testing protocols which included cell conditioning and model characterization, followed by thermal validation testing. The cell conditioning involved standard charge and discharge cycling, with standard charging at constant current, CC = C/2 (1.25 A) to 4.2 V, followed by a constant voltage stage, CV = 4.2 V until the current declined to C/50 (50 mA), whereas discharge tests were conducted at various C-rates (C/5, C/2, 1 C, and 2 C), where C-rate = C/x stands for the measurement of the charge and discharge current with respect to its nominal capacity C in a period of x hours. The conditioning protocol concluded with a low-rate constant current charge/discharge testing with two repetitive cycles at C/10 and C/25. Model characterization comprised thermodynamic testing at room temperature (23 °C) at C/100 and C/50, as well as temperature-dependent galvanostatic EIS testing at 10 °C, 20 °C, 30 °C, and 40 °C with a frequency sweep from 10 mHz to 10 kHz and a galvanostatic excitation of 0.1 A rms.

For the thermal analysis presented in this study, temperature-dependent testing schemes were carried out at 10 °C, 20 °C, 30 °C and 40 °C, which comprised two repetitive charge/discharge cycles at standard charging rates, followed by discharges at C/10, C/5, 1 C and 2 C. A 2-h rest period separated each cycle, ensuring the temperature on the cells' cases stabilized to the ambient testing temperature. Each cycling scheme was carried out individually to ensure comparability, with Cell #1 at 10 °C, Cell #2 at 20 °C, Cell #3 at 30 °C, and Cell #4 at 40 °C. This approach ensures consistent State Of Health (SOH) for each cell and scheme and optimizes the usage of laboratory testing equipment. Besides, additional tests were performed in order to assess the model's extrapolation capabilities beyond the range of characterization and operation defined initially. These comprise 1 C and 2 C discharges at 0 °C and 50 °C ambient temperatures, to cover a wider interval of potential scenarios, as well as Dynamic Stress Test (DST) at 20 °C ambient temperature, to validate model performance under dynamic conditions. The DST scheme included three complete cycles with standard charge (CC at C/2) and DST discharges with a scaled power of 250 W/kg [65], reaching a maximum of 13.63 A (5.45C rate) during discharge and 3.06 A (1.22 C rate) during charge.

The cells were tested using a calibrated multichannel Arbin battery tester LBT21044 with a resolution of 24 bits and an accuracy of ±0.02% FSR both for voltage and current measurements. Temperature measurements were conducted using ANIS MC96.1 class 1 tolerance T-type thermocouples, logged into the testing system via the Arbin's auxiliary temperature module. The cells were positioned on a high-current cylindrical cell holder from Arbin, facilitating ultra-low impedance, 4-point connections. Thermocouples were attached to the cells' cases using mounting putty. The tested cells were placed inside compressor-cooled incubators (IPC series from Memmert). Tests at 0 °C, 10 °C and 20 °C utilized the IPC450 incubator, while tests at 30 °C, 40 °C and 50 °C employed the ICP750 incubator. Despite differences in interior volume (449 L for ICP450 and 749 L for ICP750), both incubators share the same temperature range of −12 to 60 °C and a temperature setting accuracy of 0.1 °C, in accordance with standard tolerance results.

A general overview of the experimental setup and testing schemes is sketched in Fig. 2.

4. Results and discussion

All steps pertaining to model characterization and parameterization from experimental data are first described in this Section. Next, the proposed coupled electrothermal model is validated against 1 C and 2 C discharges in the range from 0 °C to 50 °C, as well as dynamic operation. A subsequent discussion on the effects of considering different modeling alternatives is presented thereafter.

4.1. Model characterization

Quasi-static behavior is characterized from thermodynamic tests at C/50 and C/100 measured at 23 °C ambient temperature, with a resulting average discharge capacity of $Q_{cell} = 2.52$ Ah. The OCV vs. SOC relationship is obtained as a linear extrapolation from thermodynamic discharge curves, as shown in Fig. 3. We assume that the calculated OCV is valid for all temperatures as its thermal variation is negligible in the range of temperatures considered in this article $|\Delta T| \leq 17\ \text{K} \ll T \sim 300\ \text{K}$; however, this thermal dependence does impact heat generation more significantly through the reversible entropic term, which is therefore considered in this article. The discharge path of the OCV vs. SOC relationship will only be employed hereafter, as experimental validation will only encompass discharge processes.

The dynamic characterization is performed in two steps. High-frequency processes, i.e. ohmic losses and charge transfer, are parameterized from full-cell EIS results at 50% SOC at 40 °C, 30 °C, 20 °C, and 10 °C. Conversely, the solid diffusion time constant is identified from full-cell discharges at C/10 and C/5 where self-heating may be safely neglected, by taking advantage of the fact that this process is only dependent on one parameter τ_d if particle capacity Q is known. This procedure is justified by the fact that experimental impedance data at very low frequency is ambiguous and may be adjusted by a multitude of frequency responses that do not necessarily match the theoretical transfer function in Eq. (2), and are also more prone to containing measurement artifacts [66]. Once electrical parameters are determined at all four ambient temperatures, an Arrhenius fit is carried out for the exchange current I_0 and the solid diffusion time constant τ_d.

Given that the solid diffusion process is characterized by a time constant τ_d several orders of magnitude slower than charge transfer dynamics, one may safely neglect the influence of this process at high frequencies. Therefore, the electrical model in Fig. 1 may be reduced to that in Fig. 4-(a), where a Constant-Phase Element (CPE) has been connected in parallel with the charge transfer resistance R_{ct} in order to model the dynamic response of the charge transfer process [8,67]. The resulting parallel connection is defined as a ZARC element, whose impedance in this case is $Z_{ct}(s) = \frac{R_{ct}}{1+(\tau_{ct}s)^{\alpha_{ct}}}$, where τ_{ct} is the charge transfer time constant and α_{ct} is the fractional-order exponent.

In consequence, high-frequency impedance data are adjusted to Eq. (14b), which is obtained by substituting $Z_1 = R_{ohm}$ and $Z_2 = \frac{R_{ct}}{1+(\tau_{ct}s)^{\alpha_{ct}}}$ in Eq. (14a) in the expression for the impedance of a discrete transmission line [46] in Fig. 4-(b). A series parasitic inductance L_p has been included with the purpose of achieving a more accurate

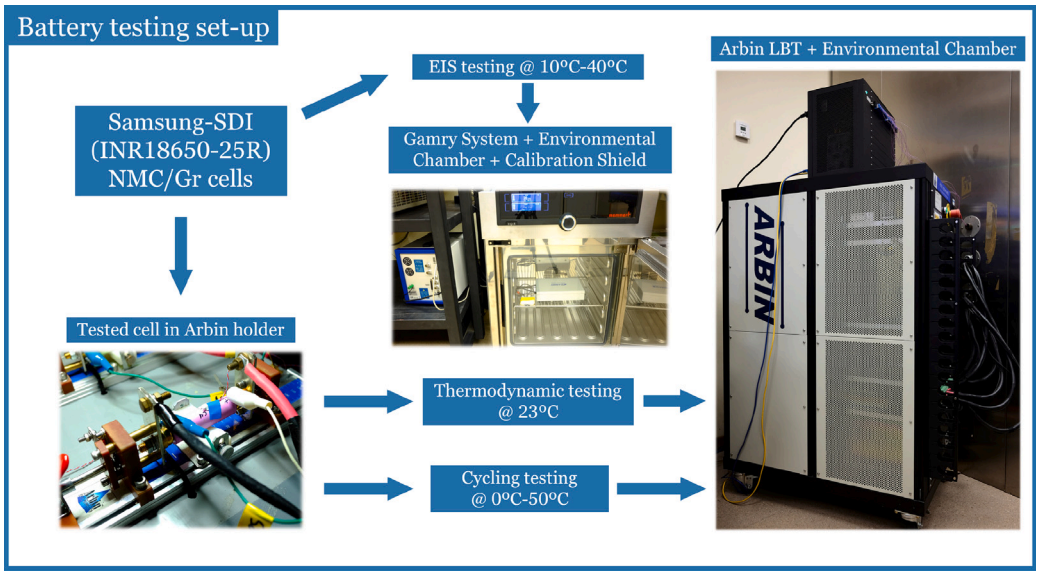

Fig. 2. Experimental setup and measurement process description.

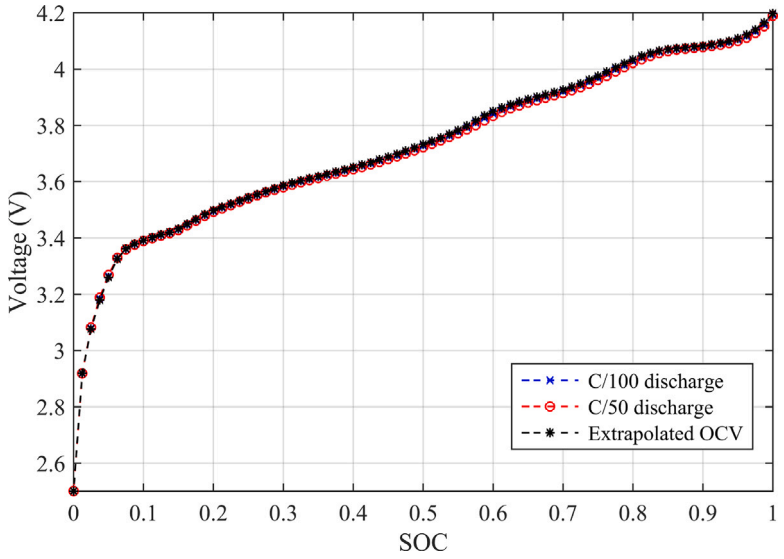

Fig. 3. Experimentally measured thermodynamic discharges along with the extrapolated OCV vs. SOC curve. Note that the calculated OCV vs. SOC relationship almost overlaps entirely with the C/100 discharge.

description of experimental data in the region of the Nyquist plot around the intersection with the real axis, in order to account for high-frequency measurement artifacts [68,69].

$$Z = \frac{Z_1}{2}\left(1 + \sqrt{1 + \frac{4Z_2}{Z_1}}\right) \tag{14a}$$

$$Z(s) = sL_p + \frac{R_{ohm}}{2}\left(1 + \sqrt{1 + \frac{4R_{ct}/R_{ohm}}{1 + (\tau_{ct}s)^{\alpha_{ct}}}}\right) \tag{14b}$$

Experimental and fitted results are depicted in Fig. 5 and shown in Table 2. A clear variation with temperature is observed in the charge transfer process, while negligible fluctuations are perceived for the ohmic resistance. The increasing asymmetry in the charge transfer impedance arc as temperature decreases is a relevant feature of Eq. (14b), and cannot be explained by a ZARC element. Although the values of τ_{ct} and α_{ct} are indicated, they are neglected for time-domain operation due to the transient response of the charge transfer process being substantially faster than the timescales in usual operation. In the mid-frequency range, no obvious impedance arc was recognizable for this particular cell [46]. Therefore, overpotentials due to concentration gradients in the electrolyte [31] are presumed to entail a less significant contribution to cell voltage; nevertheless, it was necessary to increase the ohmic resistance R_{ohm} up to 16 mΩ in order to account for R_{ce}, the resistance associated with this process.

Table 2
Summary of parameters identified from EIS data.

Temperature	R_{ohm} (mΩ)	R_{ct} (mΩ)	τ_{ct} (ms)	α_{ct}	L_s (μH)
40 °C	13.60	2.44	0.34	0.804	0.180
30 °C	13.74	6.21	0.75	0.768	0.186
20 °C	13.42	12.27	1.68	0.725	0.164
10 °C	14.19	44.13	6.50	0.754	0.148

Once the ohmic and charge transfer characteristics have been determined at all considered temperatures, discharges at C/10 and C/5 are employed in order to identify the remaining parameter τ_d for each temperature, taking advantage of the fact that at these current rates

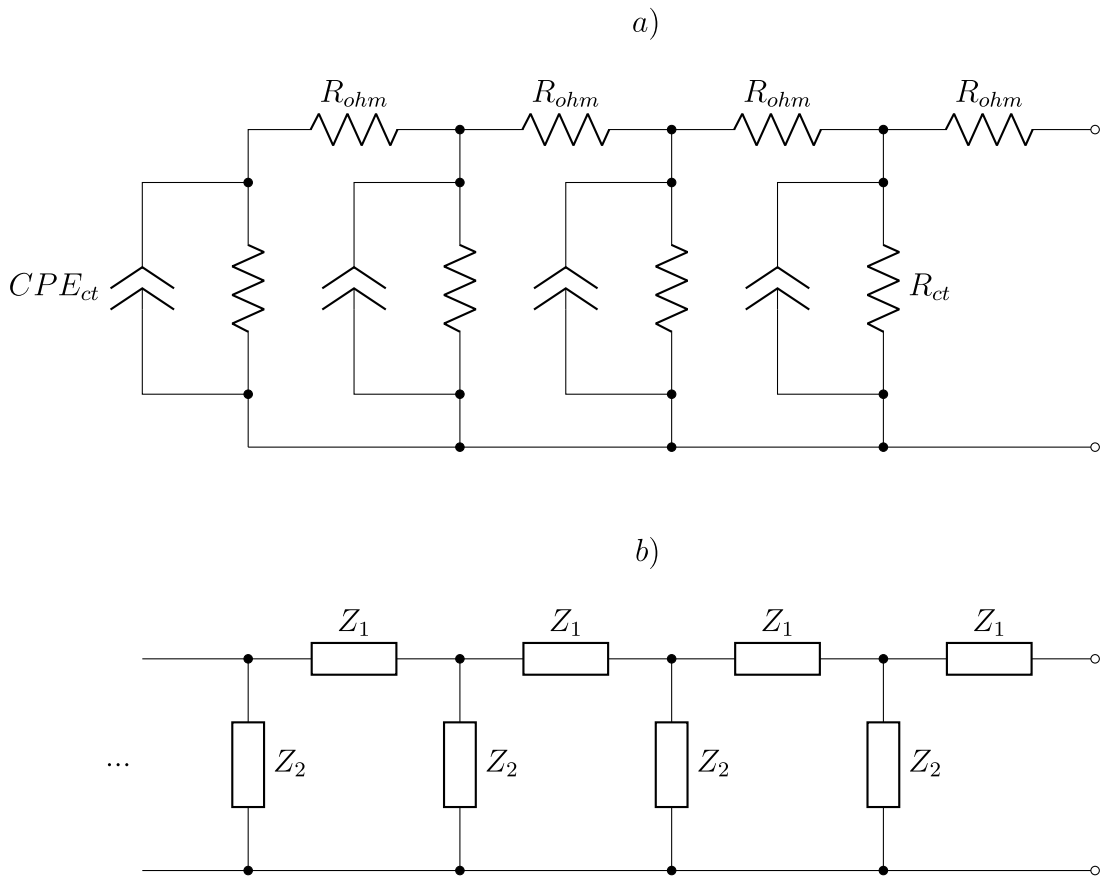

Fig. 4. (a) Equivalent circuit model for high-frequency battery impedance. (b) Discretely distributed impedance model.

Table 3
Summary of temperature-dependent parameters and Arrhenius parameters.

Temperature	10 °C	20 °C	30 °C	40 °C	A	E_a (kJ/mol)
I_0 (A)	1.099	4.117	8.427	21.081	$1.386 \cdot 10^{13}$	70.76
τ_d (s)	5190	2170	980	650	$1.228 \cdot 10^{-6}$	51.99

the heat generation is negligible [51] and parameters may safely be assumed to be constant. For this purpose, we make use of the relationship between parameters τ_d and K_d by means of particle capacity $Q_p = Q_{cell}/4$. This correlation provides a consistent and unambiguous procedure to identify parameter τ_d, since a larger time constant will also entail a greater difference between the surface and average concentrations, which will cause a vertical shift of the simulated voltage response. In consequence, a parameter sweep is performed in order to obtain a value of τ_d for each temperature that results in a high degree of agreement for both C/10 and C/5 discharges. The comparison between experimental and simulated results are shown in Fig. 6, and the identified value for τ_d at each temperature is included in Table 3.

Next, an Arrhenius fit is performed for both temperature-dependent parameters I_0 and τ_d, where I_0 is calculated from Eq. (1). This step is crucial so as to provide a functional dependency on temperature for model parameters as in Eq. (10) by using the τ_d values in Table 3, which will be required to update parameters continuously during high-rate discharges.

The Arrhenius fits for both processes are shown in Fig. 7, and the resulting parameters are summarized in Table 3.

In summary, cell capacity Q_{cell} is split evenly among the 4 active material particles, the ohmic resistance R_{ohm} has a value of 16 mΩ regardless of temperature, two parameters are used both for the temperature-dependent exchange current and solid diffusion time constant.

Lastly, the SOC dependency of entropic coefficient $K_{ent} = \frac{\partial OCV}{\partial T}$ has been determined from a literature review on this parameter in NMC/Gr cells as well as in separate electrode measurements. The entropic coefficient was measured independently for NMC and a Si/Gr composite anode in [18,59], and it was observed that a reduced amount of silicon did not substantially alter the entropy of the graphite anode [70], and the entropic coefficient corresponding to NMC was negligible with respect to that of graphite. In conclusion, the entropic heat generation is dominated by graphite, whose characteristic shape is also observed in entropic heat measurements in LFP/Gr cells [71–73].

For this reason, the confidence bands for graphite provided in [59] are employed to obtain an analytical expression based on sigmoid functions for the fit in Eq. (15), whereas the measurements in [74] for the entropic heat coefficient in a full NMC/Gr cell are taken as a reference point for stoichiometry adjustments.

$$K_{ent}(x) = 1.3x - 0.6 + \frac{2}{1+\exp(50(x-0.65))} - \frac{1.7}{1+\exp(40(x-0.4))} - \frac{5.5}{1+\exp(50(x-0.04))} \tag{15}$$

Experimental results as well as the proposed fit are shown in Fig. 8; it is noted that the entropic coefficients for graphite have taken a negative sign when translated to full cell.

Finally, thermal parameters R_{th} and τ_{th} will be identified from 1 C and 2 C discharges in the next Section, due to the fact that a sufficiently high current rate is required for the thermal response to be characterized unambiguously.

4.2. Model validation

In this Section, the presented electrothermal model is validated against experimental voltage and temperature results for 1 C and 2 C

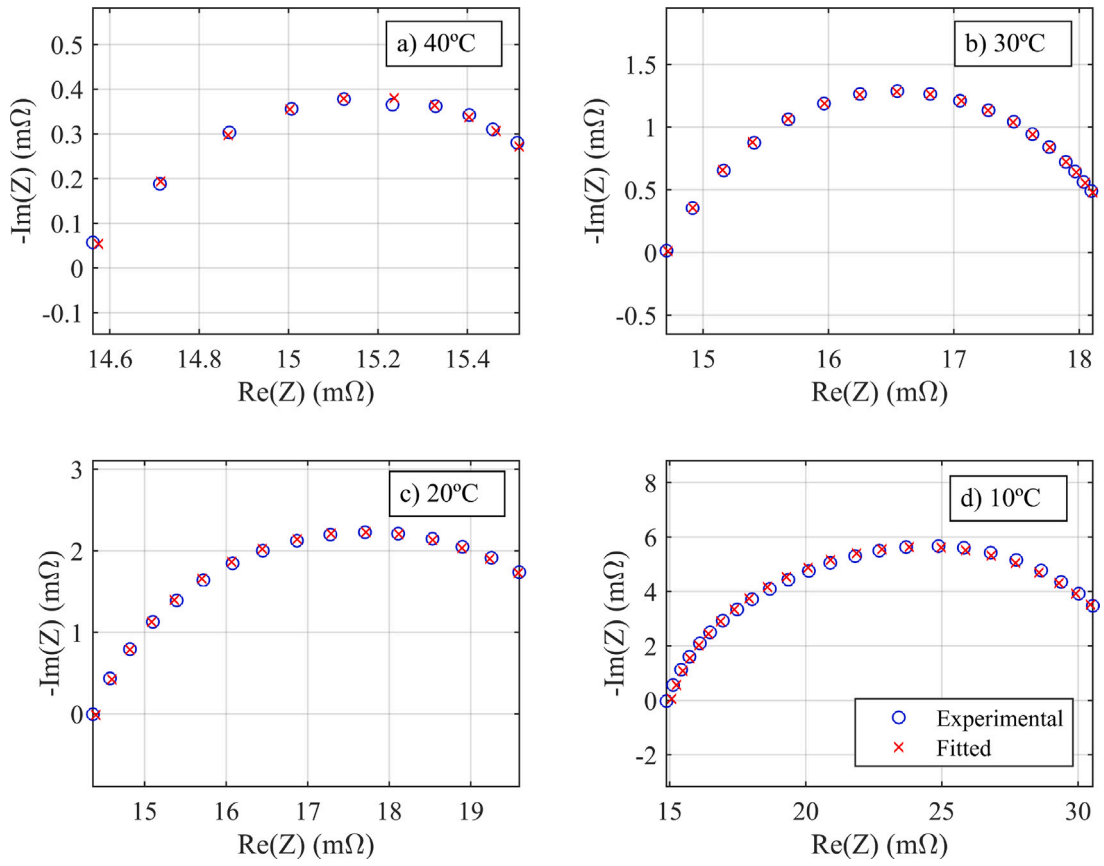

Fig. 5. Nyquist plot of experimental and fit results of high-frequency EIS data at 50% SOC at (a) 40 °C, (b) 30 °C, (c) 20 °C, and (d) 10 °C.

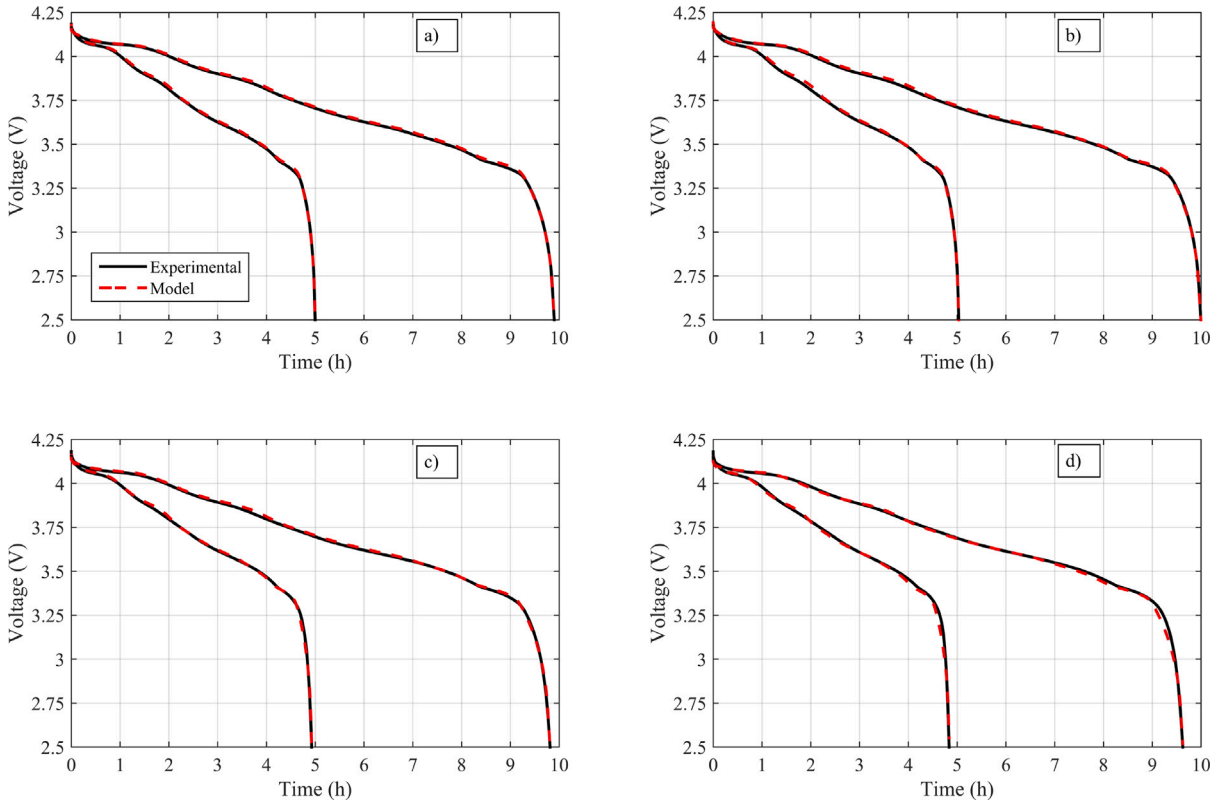

Fig. 6. Experimental and simulated results for C/10 and C/5 discharges at (a) 40 °C (τ_d = 650 s), (b) 30 °C (τ_d = 980 s), (c) 20 °C (τ_d = 2170 s), and (d) 10 °C (τ_d = 5190 s).

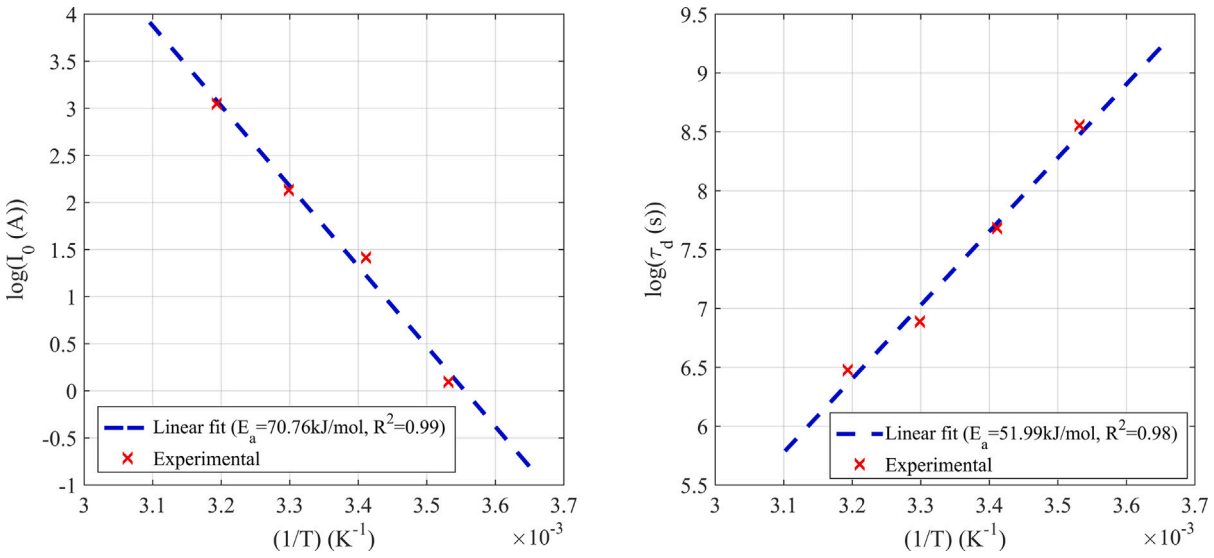

Fig. 7. Arrhenius plots for (a) the exchange current I_0 and (b) the solid diffusion time constant τ_d according to Eq. (10).

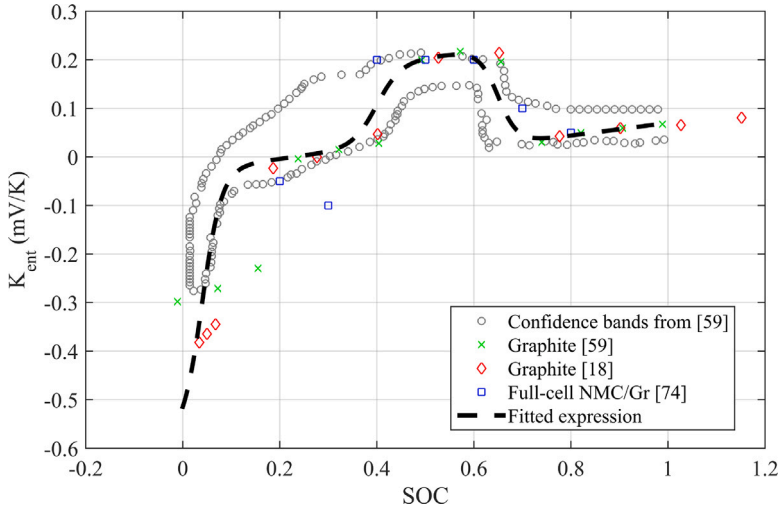

Fig. 8. Experimental measurements of the entropic coefficient from [18,59,74] and fitted expression as a function of SOC. Note that the entropic coefficients for half-cell graphite have taken a negative sign when translated to full cell.

discharges at 10 °C, 20 °C, 30 °C and 40 °C. In this article, we make the distinction between the coupled electrothermal model, in which heat generation and cell temperature are calculated from the electrical model at every timestep, and the resulting value is employed to update electrical parameters for the next timestep; and the uncoupled model in which electrical parameters are taken as constants as a function of ambient temperature only. In the case of the coupled model, the simulation timestep Δt must be selected to be sufficiently smaller than diffusion and thermal timescales so that the coupling between the different processes is effective; in this case, a $\Delta t = 0.1$ s has been defined. Thermal parameters R_{th} and τ_{th} have been identified to be 8 K/W and 750 s for tests at 30 °C and 40 °C, and 9.5 K/W and 650 s for tests at 10 °C and 20 °C, given that two separate environmental chambers with slightly different dimensions were employed to perform the aforementioned tests in parallel, as detailed in Section 3. In spite of this, the resulting values are well in line with those found in the literature for standard cylindrical-format cells [16,26,59,61,75]. Additionally, the model's extrapolation capabilities will be assessed by validating its performance against 1 C and 2 C discharges at 0 °C y 50 °C ambient temperatures, as well as dynamic schedule at 20 °C.

Output voltage, current distribution, and surface concentrations are depicted in Fig. 9 for a 2 C discharge at 40 °C, as well as the different contributions to heat generation and the simulated temperature increment, as a detailed demonstration of model operation.

It is observed that particles discharge sequentially as a function of their position instead of simultaneously, due to the presence of a macroscale distributed ohmic resistance which practically staggers the discharge process of active material particles. This is the main feature of the model in Fig. 1 with respect to Single Particle approaches. In consequence, the resulting current distribution proves to be complex: at the beginning of the discharge process, particles exhibit desynchronized discharge peaks, whereas the current distribution stabilizes due to the OCV curve being roughly linear during the mid part of the discharge. Thereafter, the curvature of the graphite Open Circuit Potential (OCP) causes the OCV-SOC curve to become nonlinear, so a more intricate current distribution emerges again. Towards the end of the discharge, the derivative of the graphite OCP is very large, so the ohmic impedance is negligible in comparison and all particles are forced to have the same surface concentration. The fluctuations in surface concentration roughly match the shape of the OCV-SOC curve, which justifies the experimentally observed smoothing effect on cell

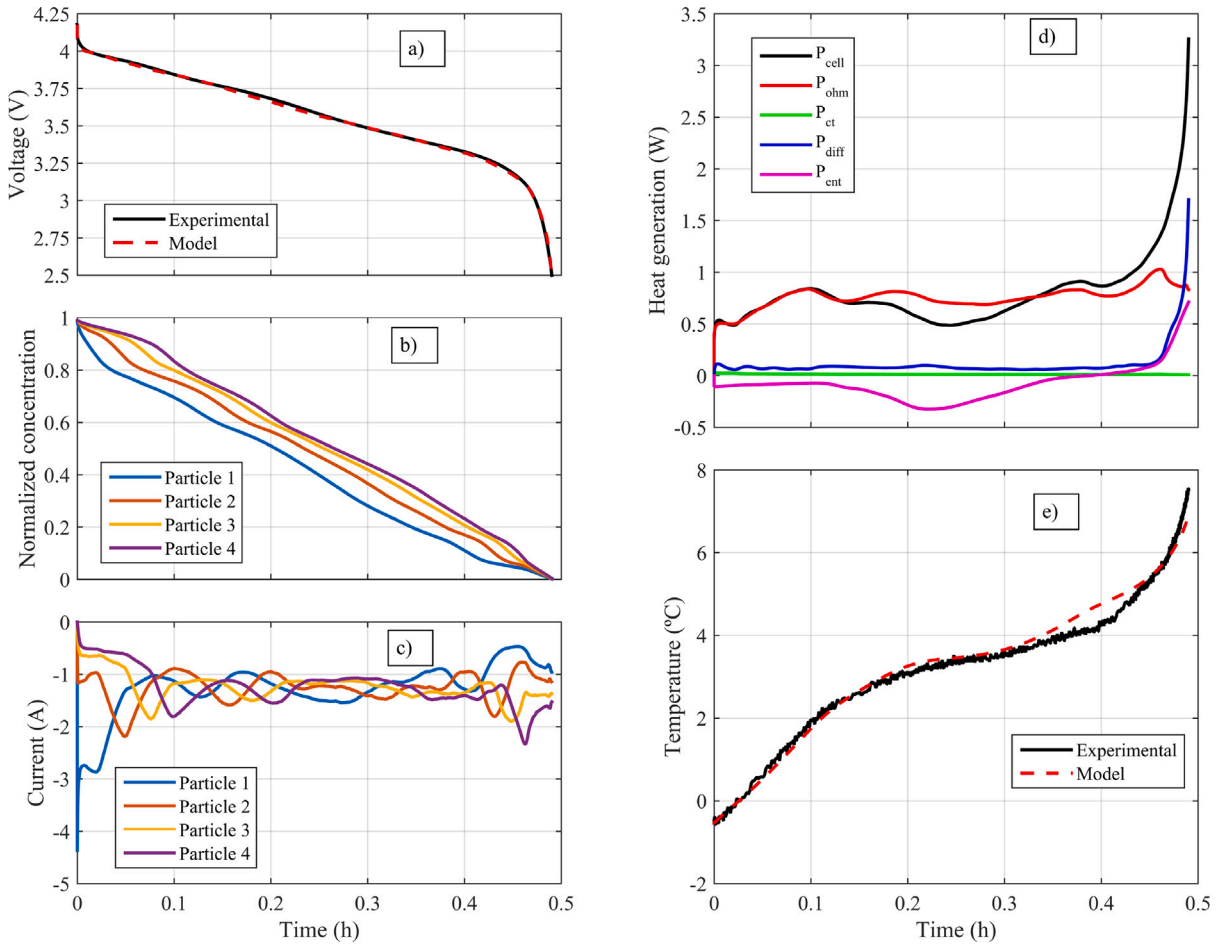

Fig. 9. Summary of simulation and experimental results for a 2 C discharge at 40 °C: (a) Experimental and model output voltage, (b) Surface concentration of active material particles, (c) Current distribution among active material particles, (d) Breakdown of heat generation terms, and (e) Temperature increase with respect to ambient temperature.

voltage. The presented model is capable of capturing this behavior, providing a close agreement with experimental data as a result.

Regarding thermal behavior, a breakdown of the different contributions to overall heat generation according to Eq. (8) is depicted, along with the temperature increase with respect to ambient temperature due to self-heating. It is noted that the heat generation due to ohmic losses is significantly greater than that of charge transfer, and the largest throughout most of the discharge, except for the final part where the gradient of the OCV-SOC curve is large, as anticipated in Section 2.2. The influence of reversible heat is the most noticeable in the middle of the discharge, where the entropic coefficient is positive and causes cell temperature to remain stable by balancing out irreversible terms. The consideration of the heat generation due to solid diffusion proves to be crucial to reproduce the temperature profile accurately throughout the complete discharge and especially during its final part, as the increasing value of the slope of the OCV-SOC curve causes a large uptick in heat generation, and cell temperature as a result, that cannot be justified otherwise. It is therefore concluded that both the entropic heat generation, as well as the heat generation due to solid diffusion, are necessary so as to explain the evolution of cell temperature during a full discharge.

A comparison between simulation and experimental results for cell voltage and temperature increase are shown in Figs. 10–13 at 40 °C, 30 °C, 20 °C, and 10 °C, respectively, whereas the RMS error is summarized in Table 4. It is observed that simulated voltage results slightly lose accuracy as ambient temperature decreases, which we mainly attribute to using effective parameters for both electrodes. In this regard, it has to be pointed out that the values for the charge transfer resistance have been identified from full-cell EIS data according to the expression for the impedance of a discrete transmission line in Eq. (14b). Nevertheless, different values may be obtained when both electrodes are considered, depending on whether the different sections of full-cell impedance are ascribed to the positive or negative electrodes, or a combination of both. The fact that accurate results are obtained with one representative electrode indicates that the ohmic resistance R_{ohm} may be evenly split between both electrodes without incurring in a large error, which may be explained by electrolyte conductivity being the limiting factor in transport along the electrode. However, experimental measurements suggest that the NMC reaction rate is significantly higher than that of graphite [16,17], so attributing the observed charge transfer resistance to the negative electrode might be more appropriate.

The proposed model may be mirrored in order to consider both electrodes separately, which would allow accounting for the dependency of the charge transfer process on concentration. However, that would render the parameterization process increasingly difficult from

Table 4
RMS error between simulation and experimental cell voltages and temperatures for 1 C and 2 C discharges at 40 °C, 30 °C, 20 °C, 10 °C ambient temperatures.

	Error in V (mV)		Error in T (°C)	
	1 C	2 C	1 C	2 C
40 °C	9.7	11.8	0.332	0.216
30 °C	11.7	17.7	0.195	0.321
20 °C	14.4	16.7	0.207	0.270
10 °C	16.5	24.8	0.24	0.674

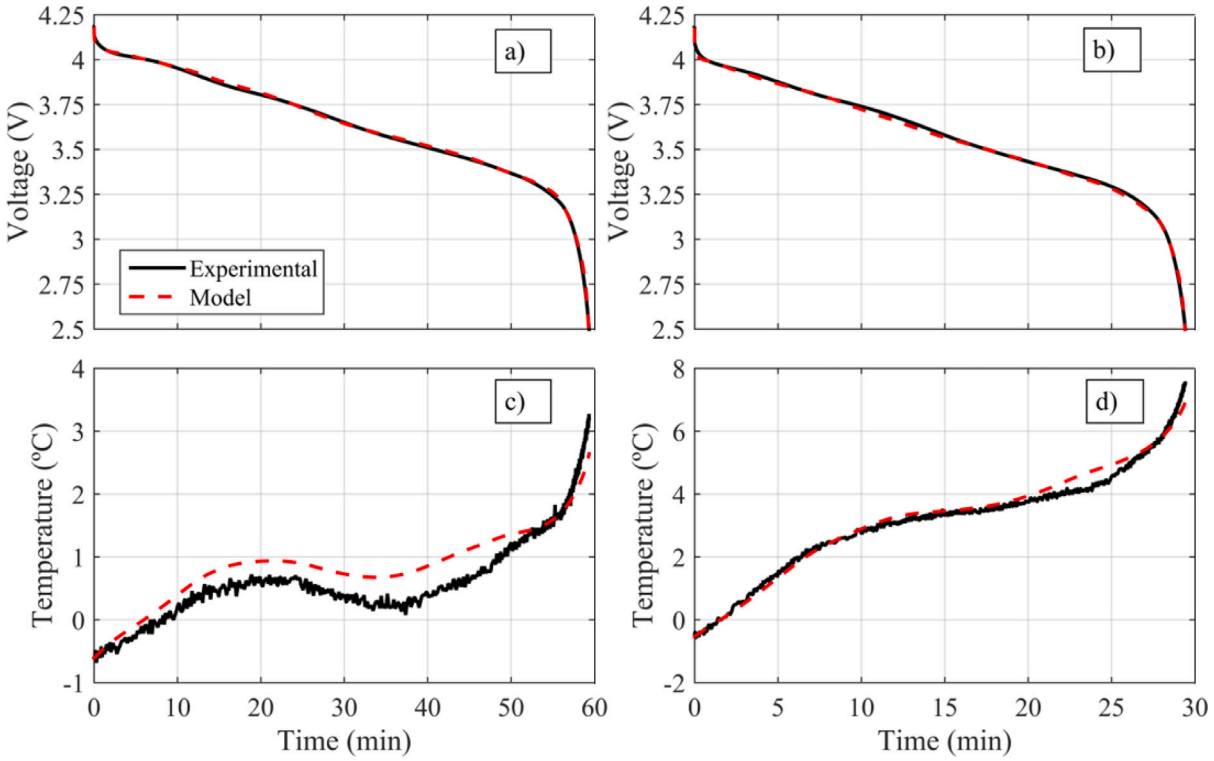

Fig. 10. Comparison between simulation (dashed line) and experimental (solid line) results for 1 C and 2 C discharges at 40 °C: (a) output voltage at 1 C and (c) temperature increase at 1 C, (b) output voltage at 2 C and (d) temperature increase at 2 C.

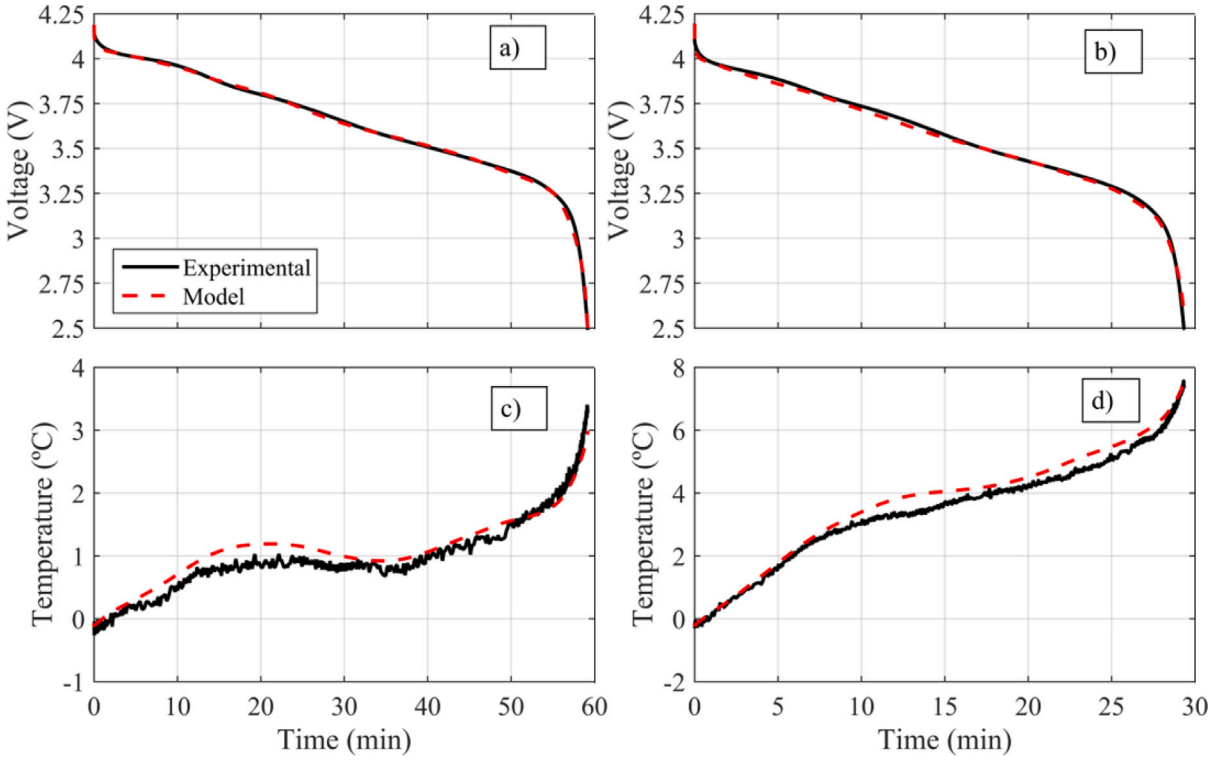

Fig. 11. Comparison between simulation (dashed line) and experimental (solid line) results for 1 C and 2 C discharges at 30 °C: (a) output voltage at 1 C and (c) temperature increase at 1 C, (b) output voltage at 2 C and (d) temperature increase at 2 C.

only full-cell experimental data, especially when activation energies E_a have to be identified separately for each process in each electrode. Nevertheless, it is noted that the proposed coupled model is able to ensure consistent behavior in a wide range of the ambient temperatures and the current rates with a unique set of constant parameters, which we understand serves to demonstrate its applicability in the most usual operating conditions. One may also notice that the least exact temperature estimation is obtained for a 2 C discharge at 10 °C ambient

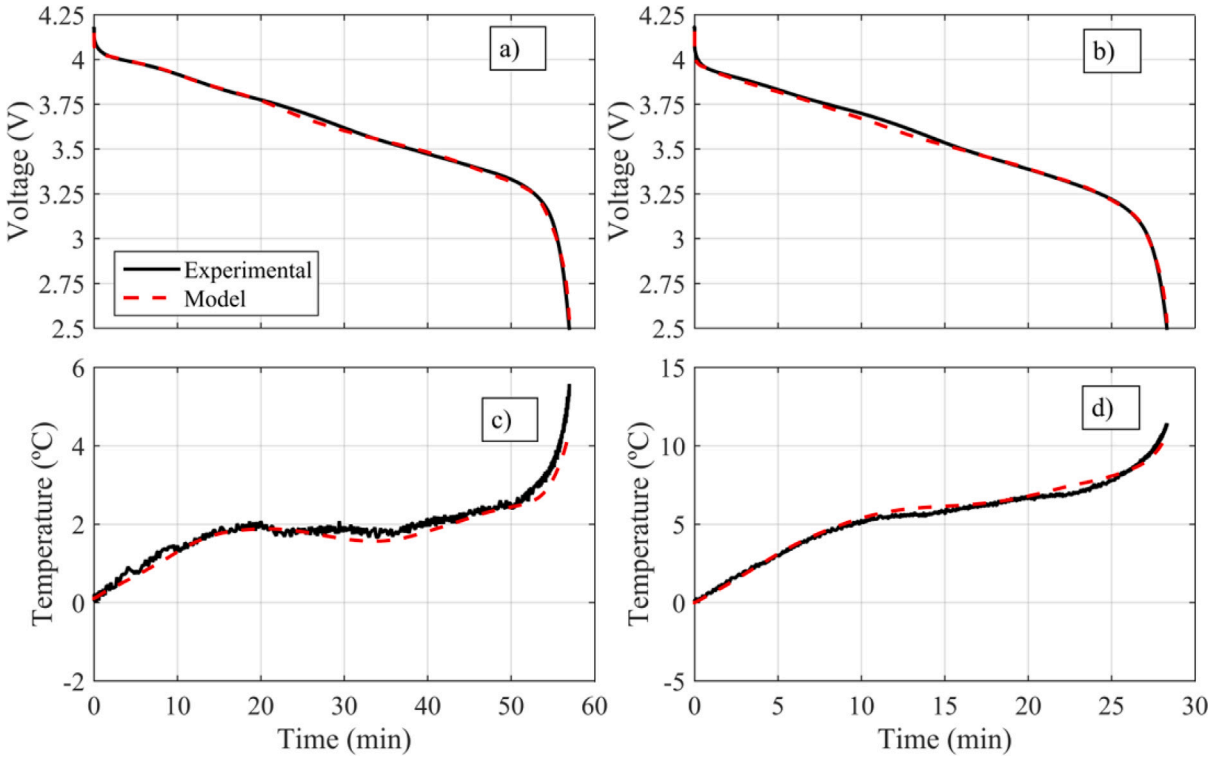

Fig. 12. Comparison between simulation (dashed line) and experimental (solid line) results for 1 C and 2 C discharges at 20 °C: (a) output voltage at 1 C and (c) temperature increase at 1 C, (b) output voltage at 2 C and (d) temperature increase at 2 C.

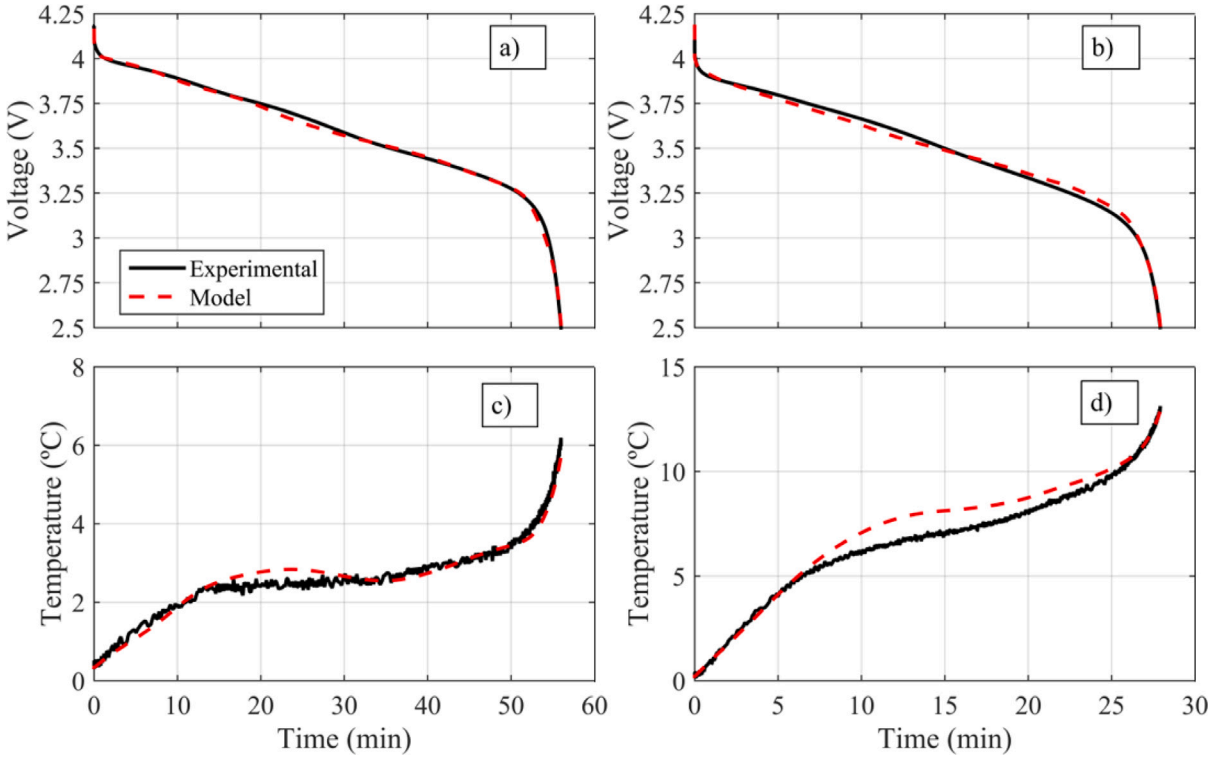

Fig. 13. Comparison between simulation (dashed line) and experimental (solid line) results for 1 C and 2 C discharges at 10 °C: (a) output voltage at 1 C and (c) temperature increase at 1 C, (b) output voltage at 2 C and (d) temperature increase at 2 C.

temperature. This is a situation where the approximation of the charge transfer process by a constant charge transfer resistance R_{ct} is not as appropriate, since parameter I_0 drastically decreases with temperature and the linearization in Eq. (1) is not as accurate as a result. In consequence, the charge transfer overpotential is overestimated during the first half of the discharge, which causes simulated cell voltage to be below the one measured experimentally, as well as excessive heat generation. Therefore, cell temperature is estimated to be slightly

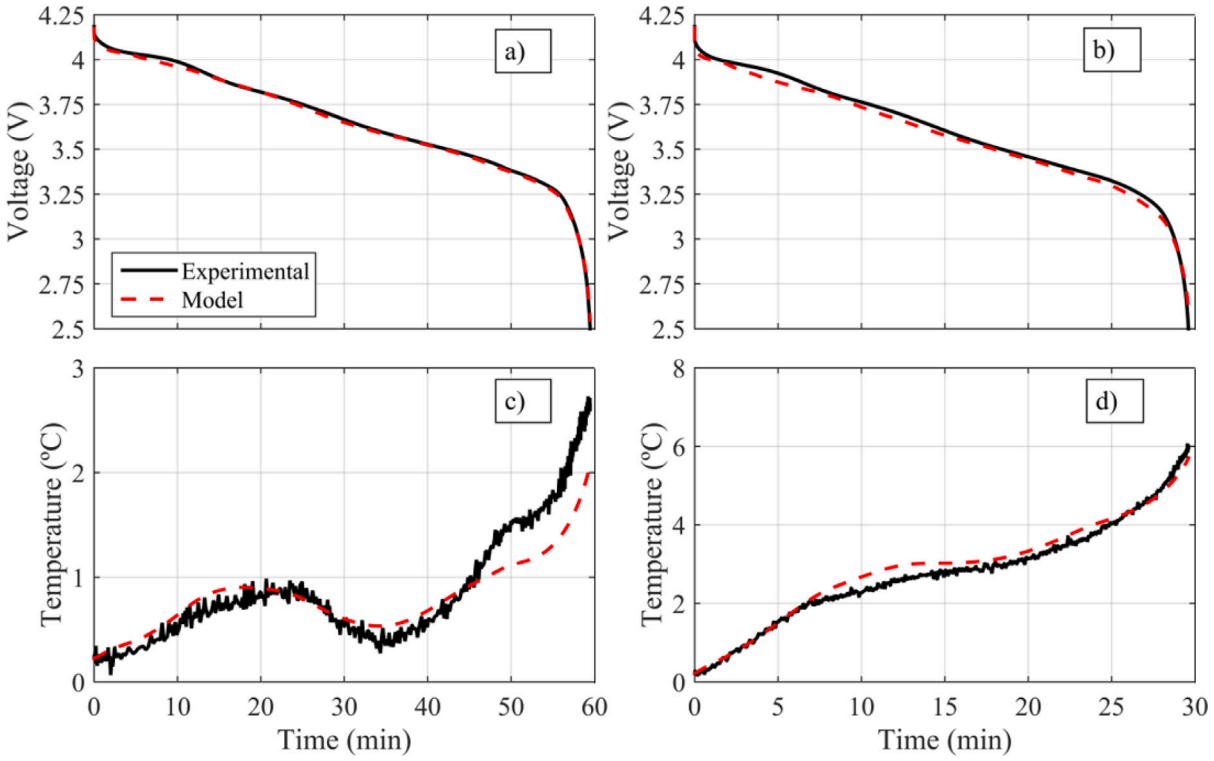

Fig. 14. Comparison between simulation (dashed line) and experimental (solid line) results for 1 C and 2 C discharges at 50 °C ambient temperature: (a) output voltage at 1 C (13.2 mV RMS) (c) temperature increase at 1 C (0.23 °C RMS), (b) output voltage at 2 C (28.9 mV RMS) (d) temperature increase at 2 C (0.22 °C RMS).

higher than indicated by experimental data. Nevertheless, the RMS error in temperature is below 0.68 °C in all cases and 0.35 °C in most, which are well within the accuracy range of the temperature sensor.

Additionally, the presented model with the same parameters determined in the previous Section is compared against experimental data from 1 C and 2 C discharges at 50 °C and 0 °C ambient temperatures, in order to assess the validity of the presented model along with the characterization procedure beyond the operating range considered initially. Results for 50 °C *y* 0 °C are depicted in Figs. 14 and 15, respectively. For the 1 C discharge at 50 °C, an accurate prediction of output voltage is obtained, whereas a qualitatively correct response is retrieved for the temperature increase, which closely resembles the shape of the entropic coefficient. This is due to the fact that in this situation, the diffusion and charge transfer overpotentials are the lowest, and the relative contribution of entropic heat is the largest. Conversely, the output voltage for the 2 C discharge presents a slightly larger deviation; nevertheless, the temperature profile is closely matched, which we believe demonstrates the importance of considering all relevant sources of heat generation.

At 0 °C ambient temperature, acceptable results are obtained, although a larger deviation is observed for output voltage. This is an expected result, since at very low temperatures, charge transfer and solid diffusion impedances grow significantly according to the Arrhenius relationship. In consequence, the differences in behavior from both electrodes are notably exacerbated, and the implicit assumption about their similar behavior imposed by the consideration of one representative electrode and OCV becomes the main source of error. However, an accurate prediction of discharge capacity is achieved in both cases, as well as a qualitative response of the temperature profile. Given that cell temperature rises to 18 °C at 2 C, we believe that a large error is avoided by employing a coupled electrothermal model and updating parameters accordingly, as parameter values at 0 °C and 20 °C differ substantially. Nevertheless, this will be discussed in greater detail in the following Section. We may conclude that, although modeling cell behavior at low temperatures warrants a separate analysis and a specific parameterization, the presented model and characterization procedures exhibit acceptable extrapolation capabilities taking into account the simplifying modeling assumptions in this article.

Finally, a comparison between simulation and experimental results is shown for a full DST discharge cycle at 20 °C ambient temperature in Fig. 16, so as to validate model performance under dynamic conditions. It is noted that highly accurate results are obtained (15.2 mV RMS for voltage and 0.14 °C RMS for temperature) throughout the whole SOC range. It is also observed that the final two discharge peaks are not completely reproduced by the model, which is the reason why the final temperature peak does not reach the same amplitude as in experimental data. As the low-SOC region is commonly considered to be mostly affected by the negative electrode, we hypothesize that a separate treatment thereof and specific parameter values may ameliorate this effect.

Although the initial justification for the discretely distributed topology stems from the observation of experimental data at constant current and different C-rates, the presented model is also fully applicable to dynamic conditions. Therefore, we may conclude that the presented ECM is a more general model with a greater range of validity, since standard ECMs may provide accurate results in dynamic operation but fail in constant-current conditions [38].

4.3. Model discussion

In this Section, different electrical and thermal modeling alternatives are considered, and their subsequent effects on model behavior are discussed, as a way to justify the modeling assumptions made in this article.

4.3.1. Lumped vs. distributed model

In this Section, we perform a comparison between the proposed electrothermal model based on a discretely distributed electrical model, and an electrothermal model based on the lumped electrical model shown in Fig. 17 [31], so as to illustrate the influence of the selected

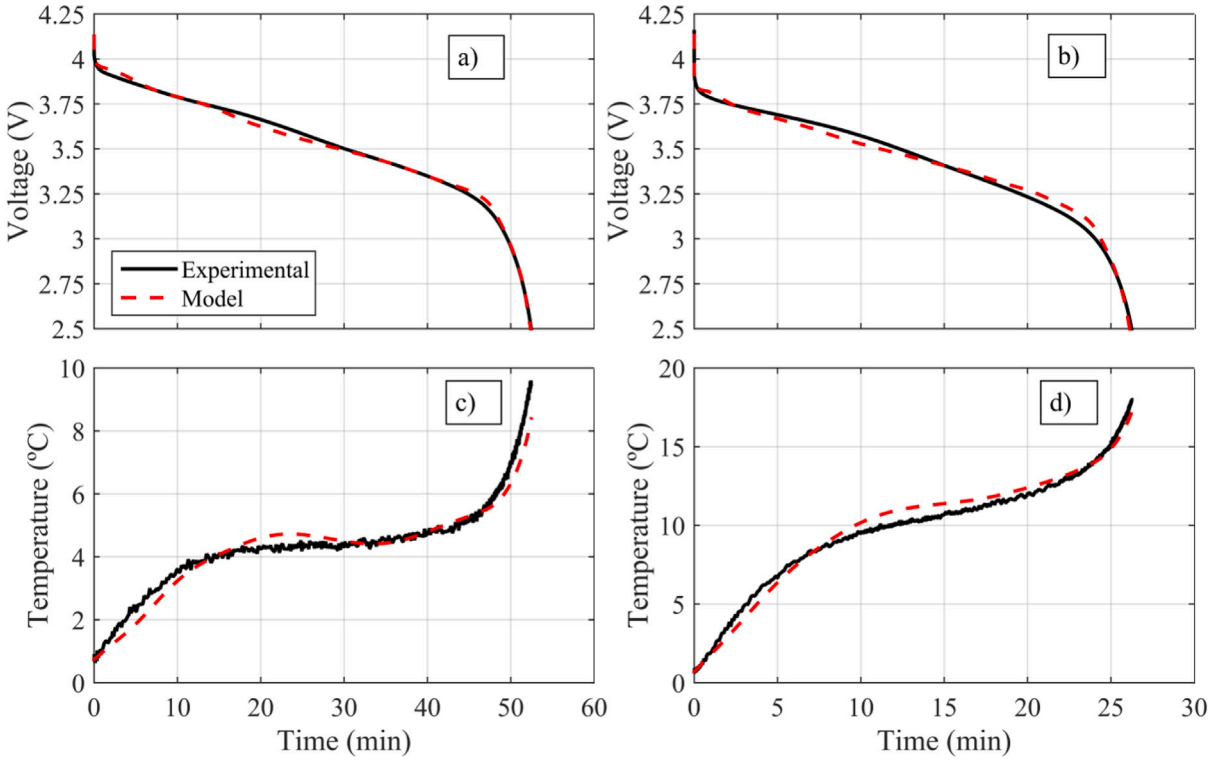

Fig. 15. Comparison between simulation (dashed line) and experimental (solid line) results for 1 C and 2 C discharges at 0 °C ambient temperature: (a) output voltage at 1 C (20.1 mV RMS) (c) temperature increase at 1 C (0.34 °C RMS), (b) output voltage at 2 C (31.6 mV RMS) (d) temperature increase at 2 C (0.55 °C RMS).

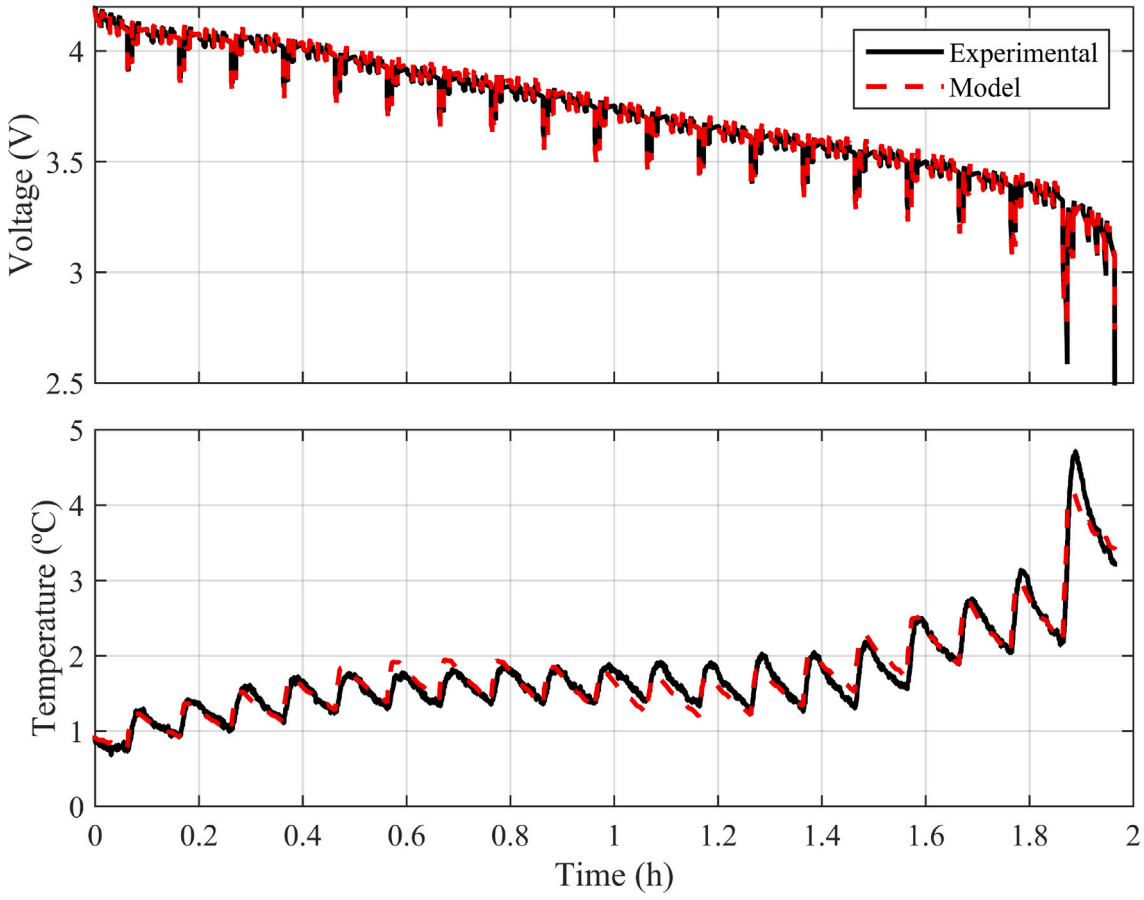

Fig. 16. Comparison between simulation (dashed line) and experimental (solid line) results for a full DST discharge cycle at 20 °C ambient temperature: (a) output voltage (15.2 mV RMS) (b) temperature increase (0.14 °C RMS).

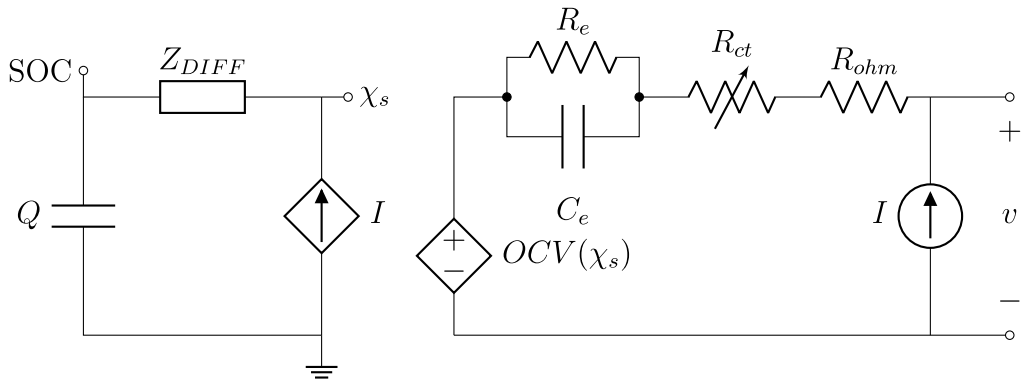

Fig. 17. Simplified equivalent circuit model from [31], in which both electrodes in the SPMe have been merged into one representative electrode.

electrical model on terminal voltage and cell temperature. The lumped ECM is the simplified version of a model that was analytically derived from the SPMe [15], where both electrodes in the SPMe have been merged into one representative electrode [37]. The leftmost section accounts for solid diffusion, while the right-hand section represents electrical behavior with the ohmic resistance, charge transfer resistance and impedance due to concentration gradients in the electrolyte.

The comparison is performed with the same electrical parameters so that discharge capacities are comparable in both cases; regarding heat generation, the lumped model in Eq. (6) is employed instead of the distributed model in (8), and thermal parameters R_{th} and τ_{th} have been adjusted for the lumped model. Simulation results are shown for 2 C discharges at 40 °C and 10 °C ambient temperatures in Fig. 18. At 40 °C, the impedances due to solid diffusion and charge transfer are significantly reduced, so the output voltage response is mostly dictated by the ohmic resistance R_{ohm}. It is noted that the lumped model is not able to reproduce the experimental voltage profile accurately as it is not smoothed out and the voltage level is mismatched. Although the voltage level throughout the discharge may be adjusted by increasing the ohmic resistance R_{ohm}, this would lead to a decrease in discharge capacity due to the abrupt slope of the OCV in the low-SOC region, and would not provide a smooth voltage curve. This effect is also visible at 10 °C, which we believe is a clear indication that the electrical model should be distributed for accurate voltage results at moderate C-rates.

As for the thermal response, apparently similar results are obtained with both models, with the distributed model providing a slightly smoother temperature profile that is also observed experimentally. However, a key aspect that must be noted is that thermal resistance R_{th} has been adjusted for the lumped model in both cases in order to provide accurate results. While its value must be increased from 8 K/W to 13.5 K/W at 40 °C, it has to be decreased from 9.5 K/W to 8.5 K/W. This is indicative of the fact that the lumped model, while being able to provide acceptable temperatures results for one specific case, cannot ensure accurate results with a consistent set of parameter values in a wider range of operating conditions, and thus, is not general enough.

A comparison of voltage error results and computation times for both the lumped and distributed model is summarized in Table 5; it is noted that the distributed model outperforms the lumped model in every case, and especially in 2 C discharges. Regarding computational cost, it is observed that the lumped model is 2–2.3 times faster for the same simulation with the same timestep of $\Delta t = 0.1$ s; this is an expected result since the distributed equivalent-circuit model contains $4 \times 4 = 16$ states, whereas the lumped model only requires 4 states. Nevertheless, an average of 44 µs per simulation timestep is obtained for the distributed model, which makes it compatible with online estimation algorithms. An advantage of this formulation of the distributed model is not having any inherent stability issues given that only one particle size is considered, and thus, the current distribution may easily be computed. However, employing an empirical OCV-SOC relationship

Table 5
Comparison between the lumped model and distributed model in voltage accuracy and computation time for 1 C and 2 C discharges at 40 °C, 30 °C, 20 °C and 10 °C ambient temperatures. Simulations were performed in MATLAB/Octave with a constant timestep of $\Delta t = 0.1$ s with an Intel Core i9-10900K processor at 3.70 GHz.

	Voltage error (mV RMS)				Computation time (s)			
	Distributed		Lumped		Distributed		Lumped	
	1 C	2 C	1 C	2 C	1 C	2 C	1 C	2 C
40 °C	9.7	11.8	38.1	60.5	1.57	0.78	0.68	0.35
30 °C	11.7	17.7	24.6	39.9	1.56	0.78	0.67	0.34
20 °C	14.4	16.7	16.4	30.1	1.51	0.75	0.65	0.32
10 °C	16.5	24.8	29.3	41.4	1.47	0.74	0.63	0.31

interpolated from experimental data (see Fig. 3) instead of a smooth analytical function may give rise to numerical instability in the region where the slope of this curve is very large, i.e. at low SOCs, which requires reducing the simulation timestep. In this article, a constant timestep of $\Delta t = 0.1$ s has been found to provide consistent results.

Therefore, we may conclude that the trade-off between accuracy and computational complexity favors the distributed electrothermal model with respect to the lumped electrothermal model, as the former provides more accurate results for cell voltage than the latter, while also allowing for a more consistent parameterization of the thermal submodel, without a major increase in computational cost.

4.3.2. Heat generation

The significance of considering the heat generation term due to the solid diffusion process, as introduced in this work, is especially noticeable at low ambient temperatures, since the time constant τ_d and its associated overpotential grow significantly according to the Arrhenius relationship. In order to highlight this aspect, the evolution of the temperature increase is also simulated without this term at 10 °C and 0 °C ambient temperature, which leads to a different resulting total heat generation, and results are shown in Figs. 19 and 20, respectively. For this purpose, thermal parameters R_{th} and τ_{th} have to be adjusted so as to compensate for a decrease in overall heat generation when the contribution of the solid diffusion is not included.

Nevertheless, it is observed that the qualitative profile and quantitative responses cannot be reproduced without taking this term into consideration for the calculation of the heat generation rate. During the middle part of the discharge reversible heat is not balanced out enough, which causes an excessive fluctuation of the estimated temperature; whereas at the end of the discharge the estimated temperature does not exhibit the observed curvature and its final uptick cannot be accounted for. Furthermore, it is not possible to achieve a close fit at both temperatures with a unique set of values for thermal parameters R_{th} and τ_{th} for the same environmental chamber, which is an indication that the contribution of solid diffusion must be included for an accurate quantification of heat generation.

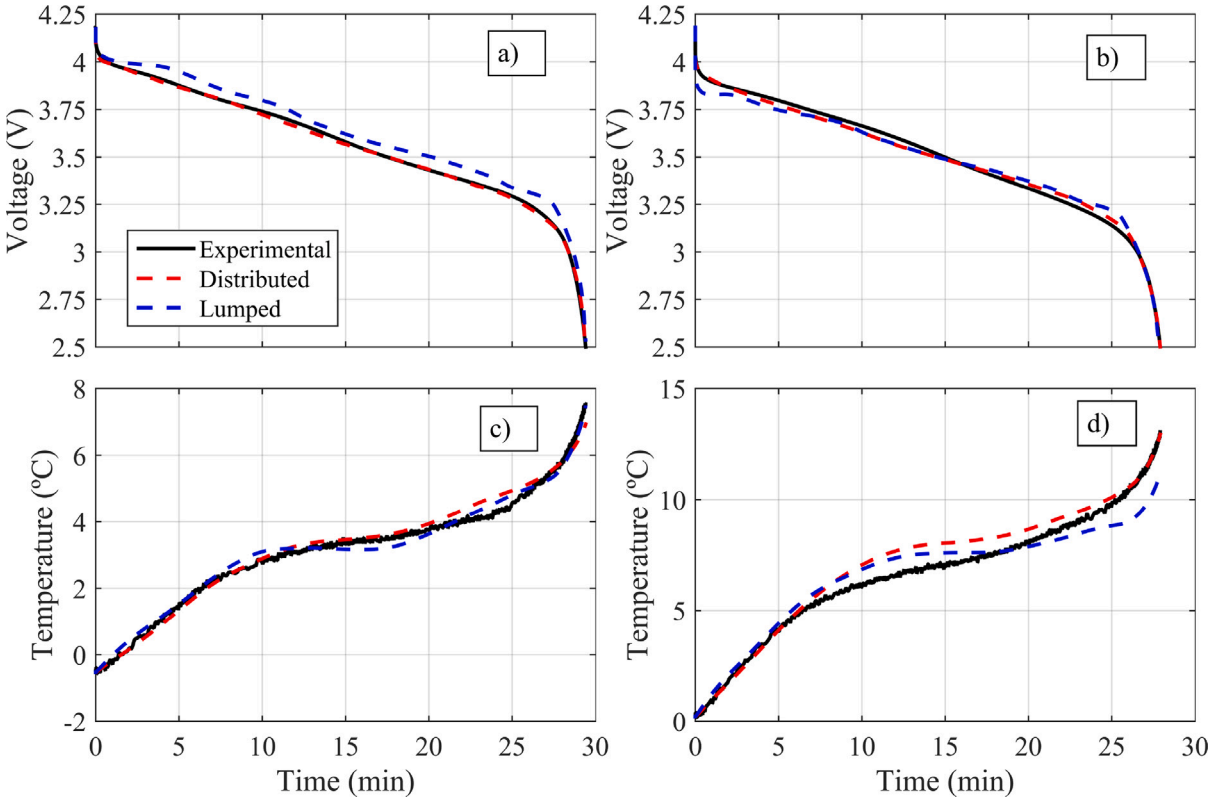

Fig. 18. Comparison between experimental (solid line) and simulation (dashed line) results for both the lumped and the distributed model for 2 C discharges at 40 °C and 10 °C ambient temperature: (a) voltage at 40 °C, (c) temperature increase at 40 °C (R_{th} = 13.5 K/W), (b) voltage at 10 °C, (d) temperature increase at 10 °C (R_{th} = 8.5 K/W).

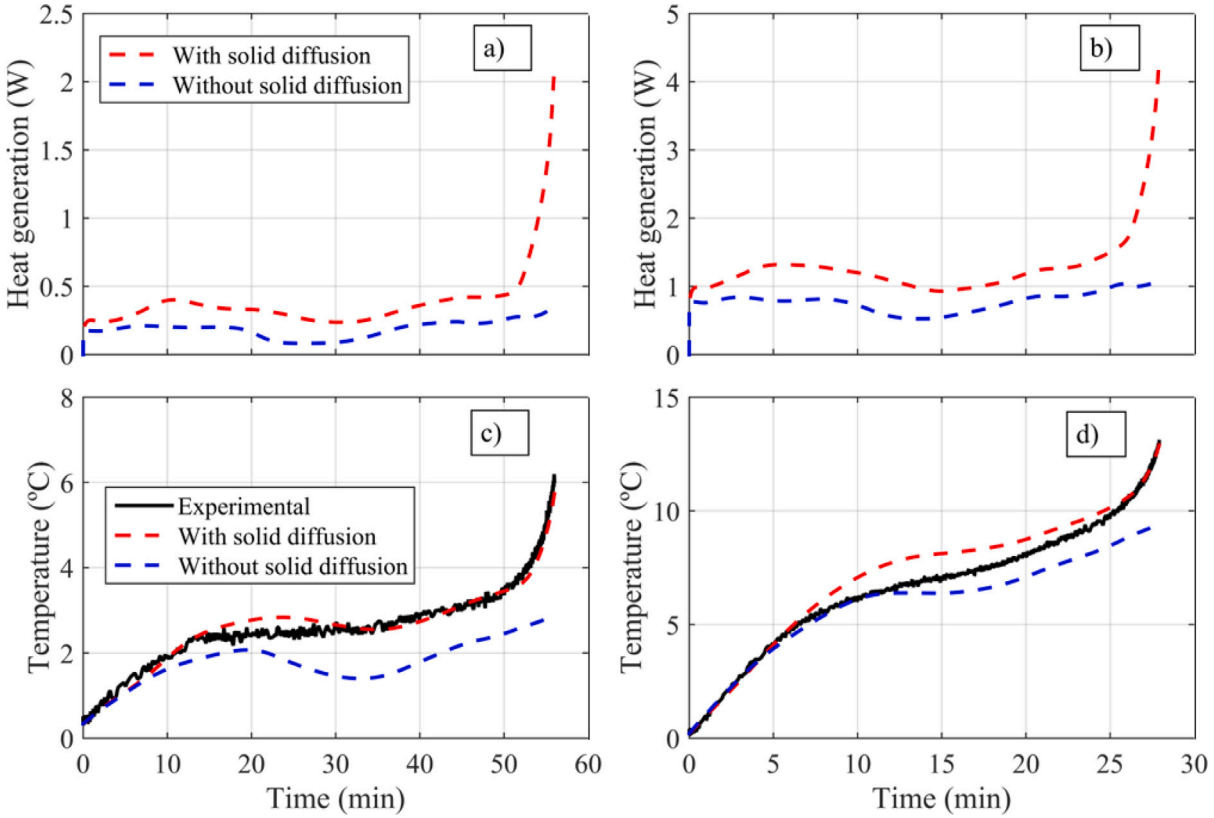

Fig. 19. Heat generation and temperature increase at 10 °C with and without the contribution of heat generation due to solid diffusion, for a 1 C discharge in (a) and (c) and a 2 C discharge in (b) and (d). Note that the thermal parameter values have been modified to 12 K/W and 600 s in the case where solid diffusion is assumed not to contribute to heat generation.

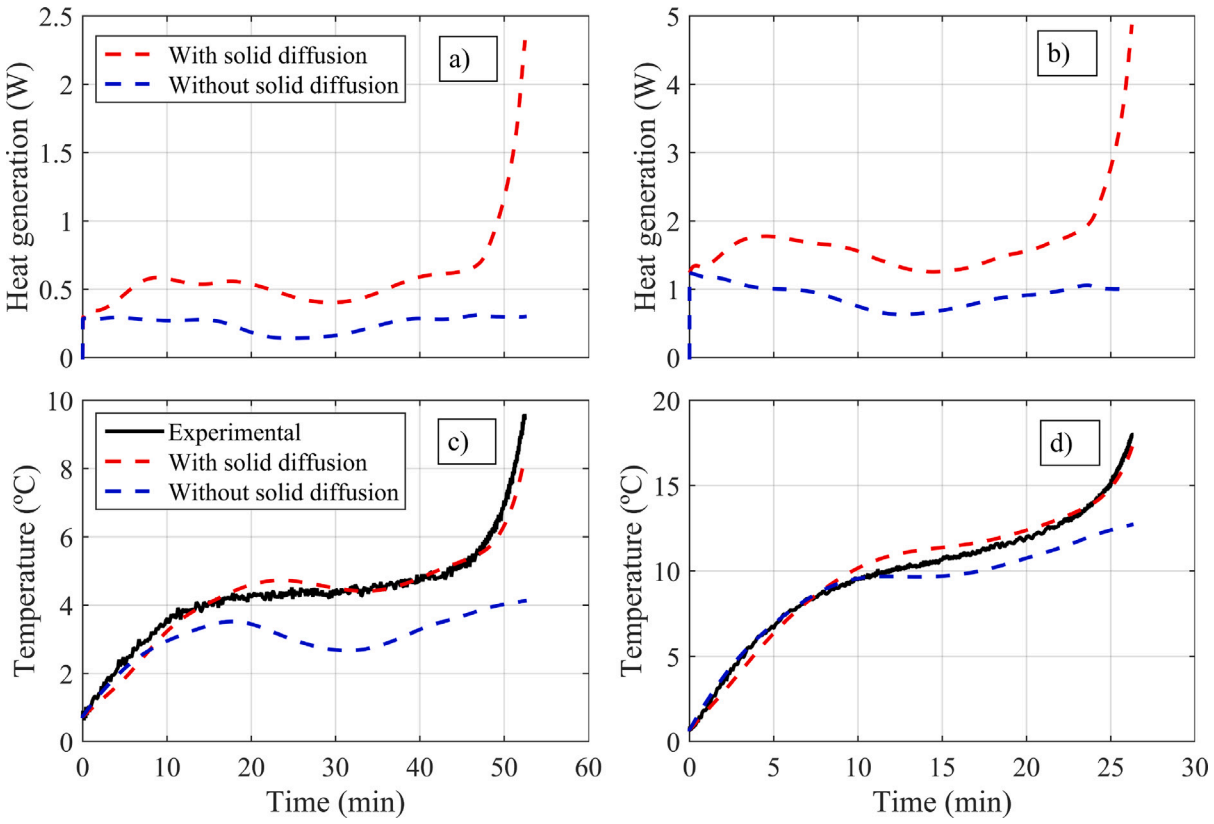

Fig. 20. Heat generation and temperature increase at 0 °C with and without the contribution of heat generation due to solid diffusion, for a 1 C discharge in (a) and (c) and a 2 C discharge in (b) and (d). Note that the thermal parameter values have been modified to 15 K/W and 600 s in the case where solid diffusion is assumed not to contribute to heat generation.

4.3.3. Electrothermal model coupling

The importance of employing a coupled electrothermal model becomes especially apparent at 10 °C ambient temperature: during 1 C and 2 C discharges, cell temperature reaches up to 6 °C and 13 °C above ambient temperature, respectively. Given the nature of the Arrhenius dependency, this difference between cell and ambient temperature will lead to parameters R_{ct} and τ_d being greater than their appropriate value, as pointed out in [19]. In order to illustrate this behavior, the operation of the model is simulated at 10 °C without a thermal model, and thus, with constant parameters values $R_{ct} = 44.13$ mΩ and $\tau_d = 5190$ s identified in the previous Section. The comparison between experimental data and simulation results for the coupled and uncoupled models is shown in Fig. 21 for 1 C and 2 C discharges. In both cases, the uncoupled model presents a larger impedance than appropriate, which causes output voltage to drop excessively and reach the lower cutoff limit sooner than observed experimentally. The temperature increase starts being significant about 40 min in the 1 C discharge, where the simulation results provided by both models start to deviate; the extracted capacity in both cases is 2.33 Ah vs. 2.25 Ah. Conversely, at 2 C, cell temperature exceeds 15 °C for most of the discharge; therefore, the discrepancy between the output voltages provided by both models is noticeable throughout the complete process. In this case, the charge throughputs are 2.32 Ah vs. 2.05 Ah, which is a considerable difference of about 12% in capacity.

This trend is exacerbated even further at 0 °C ambient temperature, as shown in Fig. 22, since cell temperature reaches up to 9.5 °C and 18 °C above ambient temperature, respectively. In this case, the extracted capacities are 1.99 Ah vs. 2.19 Ah at 1 C (8.9% difference), and 1.58 Ah vs. 2.18 Ah at 2 C (27.4% difference). This is a clear indication that a coupled electrothermal model is required at low ambient temperatures, as self-heating causes cell temperature to differ significantly from ambient temperature, and a large error is committed if model parameters are not updated accordingly. This modeling approach is able to provide an accurate estimation of discharge capacity in a wide range of operating conditions without artificial adjustments with temperature and current rate (see Fig. 22).

Finally, a thorough discussion on model shortcomings and future extensions is provided. Regarding electrical modeling aspects, the main limitation of the presented model in its current state lies in the assumption of similar properties for both electrodes in order to merge them into one representative electrode. This hypothesis greatly simplifies the characterization process from non-destructive experimental data, since the number of parameters to be determined is halved, and an experimental OCV-SOC relationship may be employed instead of electrode OCPs. Nevertheless, this assumption is not necessarily true, and we believe this is the main reason for deviations at low temperatures. In consequence, a direct extension of this work is treating electrodes separately and determining individual parameters and thermal dependencies. Moreover, a distribution of particle sizes may also be incorporated so as to analyze voltage relaxation profiles, as well as making the required considerations to extend model applicability beyond 2 C [19]. However, we would like to point out that the experimental validation has been performed with a unique parameter set for all cases, which proves its applicability.

As for thermal modeling, shortcomings arise from the assumption of homogeneous cell temperature. Although a common premise, especially in cylindrical small-format cells, it is a clear simplification of temperature gradients occurring within the cell. However, as stated in Section 2.2, there is not a clear correlation between the radial cell dimension and the electrode spatial dimension. Therefore, considering cell temperature gradients would require developing a 3D model of electrode structure [29], which then should be coupled with a heat transfer model inside the cell. We believe that this would

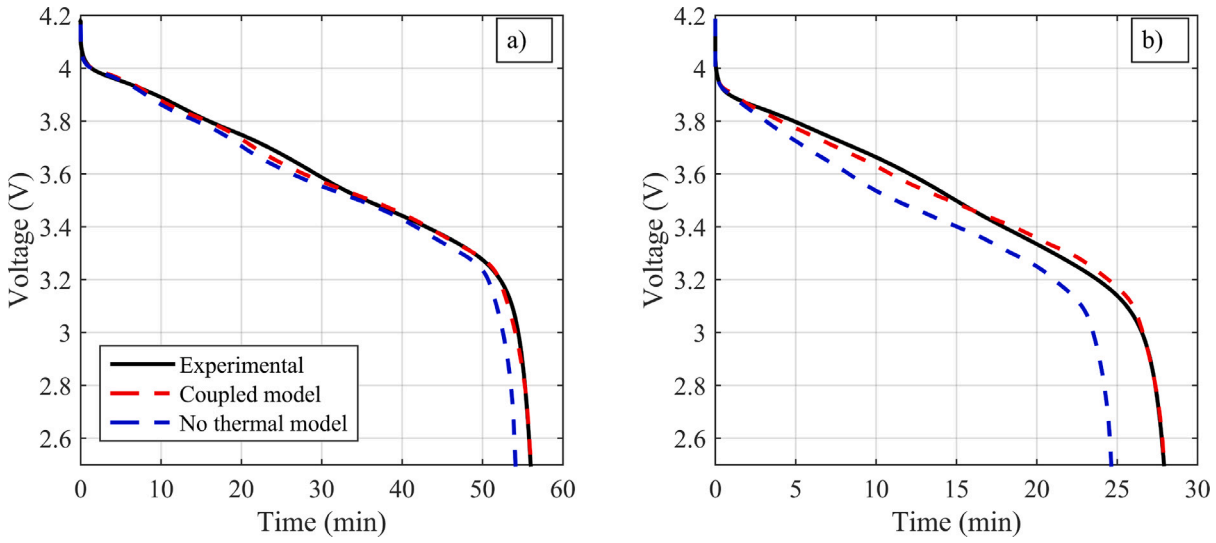

Fig. 21. Simulation (dashed lines) and experimental (solid line) output voltage results for discharges at 10 °C at (a) 1 C and (b) 2 C with and without a coupled thermal model.

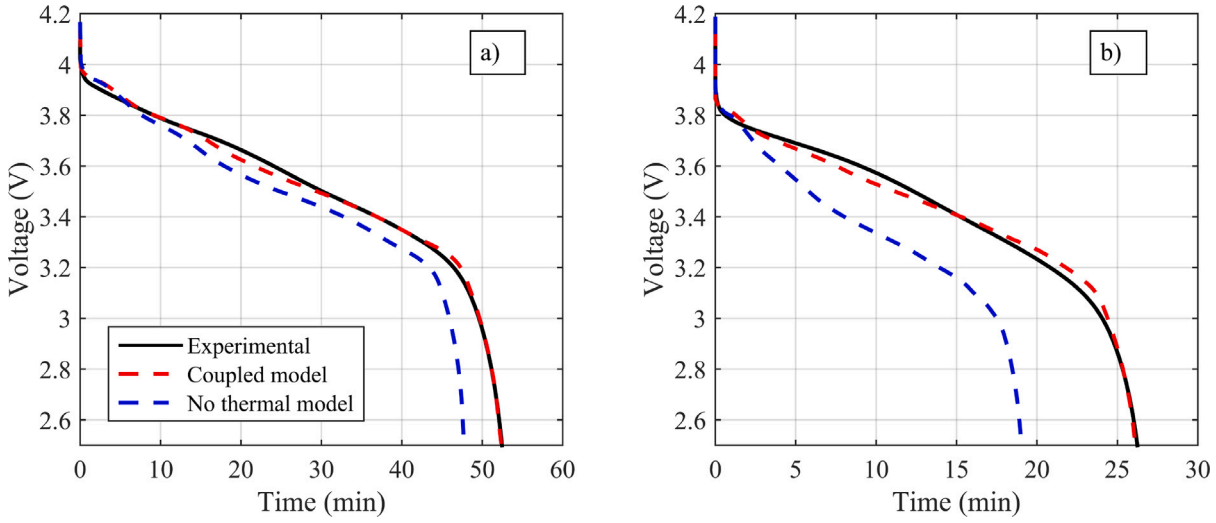

Fig. 22. Simulation (dashed lines) and experimental (solid line) output voltage results for discharges at 0 °C at (a) 1 C and (b) 2 C with and without a coupled thermal model.

be challenging and computationally intensive, as well as not suitable for practical applications. Moreover, physical properties such as cell thermal conductivity are hard to determine uniquely and show high dispersion [76]. Assuming a homogeneous temperature may lead to inaccuracies at very high current rates that cause a considerable temperature gradient, as well as in large-format cell geometries or battery packs for which there is not a uniform ambient temperature. Although the main focus of the article is on heat generation and the influence of temperature on output voltage, we believe that another possible extension is the combination of the present electrical and heat generation model with a more sophisticated thermal model. We also consider that a promising line of research would be the development of isothermal testing setups that are able to maintain a constant cell temperature compensating for self-heating through heat dissipation or forced ventilation. In this manner, thermal effects may be decoupled from purely electrical behavior, which would also allow validating or disproving modeling hypotheses more conclusively.

5. Conclusions

In this article, a novel coupled electrothermal model has been developed so as to explain cell behavior in a wide range of ambient temperatures and current rates with a unique set of constant parameters. The proposed model employs a single-electrode, discretely distributed topology, which provides an excellent trade-off between accuracy and parameterization complexity in practical operating conditions. The thermal dependencies of electrical parameters are identified from experimental EIS and low-rate discharge data, and then fitted to respective Arrhenius equations. A key contribution of this work is the identification of all relevant sources of heat generation, including entropic heat and heat generation due to solid diffusion, which proves to be essential in order to qualitatively and quantitatively explain the evolution of cell temperature. The presented electrothermal model is capable of providing highly accurate results both in output voltage (≤25 mV RMS) and cell temperature (≤0.68 °C RMS) at a low computational cost with a set of 7 well-defined parameters, in the interval from 40 °C to 10 °C ambient temperatures. Additionally, an acceptable extrapolation capability is demonstrated at 50 °C and 0 °C ambient temperatures. The coupling between the thermal and the electrical model is shown to be especially crucial at low ambient temperatures, where cell impedance is the largest and the influence of self-heating is the most significant. Further extensions of this work comprise the development of parameterization methodologies when both electrodes are considered separately, as well as model adjustments for higher current rates. Nevertheless, we believe that the proposed model in

Table A.6
Abbreviations.

Abbreviation	Description
BMS	Battery Management System
BTMS	Battery Thermal Management System
CC-CV	Constant Current - Constant Voltage
CPE	Constant-Phase Element
DFN	Doyle–Fuller–Newman
DRT	Distribution of Relaxation Times
DST	Dynamic Stress Test
ECM	Equivalent Circuit Model
EIS	Electrochemical Impedance Spectroscopy
LIB	Lithium-ion battery
NMC811	Nickel–Manganese–Cobalt (811)
OCP	Open Circuit Potential
OCV	Open Circuit Voltage
RMS	Root Mean Square
SOC	State Of Charge
SPM	Single-Particle Model
SPMe	Single Particle Model with electrolyte dynamics

its current formulation constitutes a suitable alternative for practical applications.

CRediT authorship contribution statement

Pablo Rodríguez-Iturriaga: Methodology, Investigation, Formal analysis, Data curation, Conceptualization, Software, Visualization, Writing – original draft, Writing – review & editing. **Víctor Manuel García:** Formal analysis, Investigation, Methodology, Supervision, Writing – original draft, Writing – review & editing. **Salvador Rodríguez-Bolívar:** Formal analysis, Funding acquisition, Investigation, Methodology, Project administration, Software, Supervision, Writing – review & editing. **Enrique Ernesto Valdés:** Data curation, Methodology, Resources, Validation. **David Anseán:** Data curation, Funding acquisition, Methodology, Project administration, Resources, Validation, Writing – original draft, Writing – review & editing. **Juan Antonio López-Villanueva:** Formal analysis, Funding acquisition, Investigation, Methodology, Project administration, Software, Supervision, Validation, Writing – review & editing.

Declaration of competing interest

The authors declare that they have no known competing financial interests or personal relationships that could have appeared to influence the work reported in this paper.

Data availability

Data will be made available on request.

Acknowledgments

This work was partially supported by the Spanish Ministry of Science and Innovation via Project PID2022-141792OB-I00, by the Principality of Asturias via project AYUD/2021/50994, and by the Vice-Rectorate for Research and Knowledge Transfer at University of Granada via Applied Research Project C-ING-188-UGR23. Pablo Rodríguez-Iturriaga acknowledges grant FPU22/00501 by the Spanish Ministry of Science and Innovation.

Appendix A. Abbreviations

See Table A.6.

Appendix B. Nomenclature

See Table B.7.

Table B.7
Nomenclature.

Symbol	Description (Units)
R_s	Active material particle radius (m)
D_s	Solid diffusivity (m^2/s)
A	Electrode area (m^2)
I_0	Exchange current (A)
η_r	Charge transfer overpotential (V)
χ_s	Normalized surface concentration in active material particles
$\overline{\chi}$	Normalized average concentration in active material particles
F	Faraday's constant (C/mol)
R	Universal gas constant (J K^{-1} mol^{-1})
T	Temperature (K)
R_{ct}	Charge-transfer resistance (Ω)
R_{ohm}	Ohmic resistance (Ω)
R_{th}	Thermal resistance (K/W)
τ_{th}	Thermal time constant (s)
Q_C	Cell capacity (Ah)
Q_n	Particle capacity (Ah)
K_d	Solid diffusion gain (A^{-1})
τ_d	Solid diffusion time constant (s)
τ_{ref}	Reference solid diffusion time constant (s)
τ_{ct}	Charge transfer time constant (s)
α_{ct}	Charge transfer order exponent
L_p	Series parasitic inductance (H)
Z_{DIFF}	Solid diffusion impedance after subtracting integrator dynamics (Ω)

References

[1] Zhao C, Andersen PB, Trætholt C, Hashemi S. Grid-connected battery energy storage system: a review on application and integration. Renew Sustain Energy Rev 2023;182:113400. http://dx.doi.org/10.1016/j.rser.2023.113400.

[2] Baigorri J, Zaversky F, Astrain D. Massive grid-scale energy storage for next-generation concentrated solar power: A review of the potential emerging concepts. Renew Sustain Energy Rev 2023;185:113633. http://dx.doi.org/10.1016/j.rser.2023.113633.

[3] Xie J, Lu Y-C. A retrospective on lithium-ion batteries. Nature Commun 2020;11:2499. http://dx.doi.org/10.1038/s41467-020-16259-9.

[4] Ma S, Jiang M, Tao P, Song C, Wu J, Wang J, Deng T, Shang W. Temperature effect and thermal impact in lithium-ion batteries: A review. Prog Natl Sci: Mater Int 2018;28(6):653–66. http://dx.doi.org/10.1016/j.pnsc.2018.11.002.

[5] Pozzato G, Allam A, Pulvirenti L, Negoita GA, Paxton WA, Onori S. Analysis and key findings from real-world electric vehicle field data. Joule 2023;7(9):2035–53. http://dx.doi.org/10.1016/j.joule.2023.07.018.

[6] Ruan H, Barreras JV, Steinhardt M, Jossen A, Offer GJ, Wu B. The heating triangle: A quantitative review of self-heating methods for lithium-ion batteries at low temperatures. J Power Sources 2023;581:233484. http://dx.doi.org/10.1016/j.jpowsour.2023.233484.

[7] Wang Y, Tian J, Sun Z, Wang L, Xu R, Li M, Chen Z. A comprehensive review of battery modeling and state estimation approaches for advanced battery management systems. Renew Sustain Energy Rev 2020;131:110015. http://dx.doi.org/10.1016/j.rser.2020.110015.

[8] Carthy KM, Gullapalli H, Ryan KM, Kennedy T. Review—use of impedance spectroscopy for the estimation of Li-Ion battery state of charge, state of health and internal temperature. J Electrochem Soc 2021;168(8):080517. http://dx.doi.org/10.1149/1945-7111/ac1a85.

[9] Talele V, Moralı U, Patil MS, Panchal S, Fraser R, Fowler M, Thorat P, Gokhale YP. Computational modelling and statistical evaluation of thermal runaway safety regime response on lithium-ion battery with different cathodic chemistry and varying ambient condition. Int Commun Heat Mass Transfer 2023;146:106907. http://dx.doi.org/10.1016/j.icheatmasstransfer.2023.106907.

[10] Singh LK, Kumar R, Gupta AK, Sharma A, Panchal S. Computational study on hybrid air-PCM cooling inside lithium-ion battery packs with varying number of cells. J Energy Storage 2023;67:107649. http://dx.doi.org/10.1016/j.est.2023.107649.

[11] Baveja R, Bhattacharya J, Panchal S, Fraser R, Fowler M. Predicting temperature distribution of passively balanced battery module under realistic driving conditions through coupled equivalent circuit method and lumped heat dissipation method. J Energy Storage 2023;70:107967. http://dx.doi.org/10.1016/j.est.2023.107967.

[12] Mastali M, Farkhondeh M, Farhad S, Fraser RA, Fowler M. Electrochemical modeling of commercial LiFePO4 and graphite electrodes: Kinetic and transport properties and their temperature dependence. J Electrochem Soc 2016;163(13):A2803. http://dx.doi.org/10.1149/2.1151613jes.

[13] Miguel E, Plett GL, Trimboli MS, Oca L, Iraola U, Bekaert E. Review of computational parameter estimation methods for electrochemical models. J Energy Storage 2021;44:103388. http://dx.doi.org/10.1016/j.est.2021.103388.

[14] Rabissi C, Sordi G, Innocenti A, Casalegno A. Fast and reliable calibration of thermal-physical model of lithium-ion battery: a sensitivity-based method. J Energy Storage 2023;59:106435. http://dx.doi.org/10.1016/j.est.2022.106435.

[15] Marquis SG, Sulzer V, Timms R, Please CP, Chapman SJ. An Asymptotic Derivation of a Single Particle Model with Electrolyte. J Electrochem Soc 2019;166(15):A3693–706. http://dx.doi.org/10.1149/2.0341915jes.

[16] Brosa Planella F, Sheikh M, Widanage WD. Systematic derivation and validation of a reduced thermal-electrochemical model for lithium-ion batteries using asymptotic methods. Electrochim Acta 2021;388:138524. http://dx.doi.org/10.1016/j.electacta.2021.138524.

[17] Chen C-H, Planella FB, O'Regan K, Gastol D, Widanage WD, Kendrick E. Development of experimental techniques for parameterization of multi-scale lithium-ion battery models. J Electrochem Soc 2020;167(8):080534. http://dx.doi.org/10.1149/1945-7111/ab9050.

[18] O'Regan K, Brosa Planella F, Widanage WD, Kendrick E. Thermal-electrochemical parameters of a high energy lithium-ion cylindrical battery. Electrochim Acta 2022;425:140700. http://dx.doi.org/10.1016/j.electacta.2022.140700.

[19] Wang L, Jin M, Cai Y, Lian Y, Zhao X, Wang R, Qiao S, Chen L, Yan X. Construction of electrochemical model for high C-rate conditions in lithium-ion battery based on experimental analogy method. Energy 2023;279:128073. http://dx.doi.org/10.1016/j.energy.2023.128073.

[20] Bruch M, Millet L, Kowal J, Vetter M. Novel method for the parameterization of a reliable equivalent circuit model for the precise simulation of a battery cell's electric behavior. J Power Sources 2021;490:229513. http://dx.doi.org/10.1016/j.jpowsour.2021.229513.

[21] Pang H, Guo L, Wu L, Jin J, Zhang F, Liu K. A novel extended Kalman filter-based battery internal and surface temperature estimation based on an improved electro-thermal model. J Energy Storage 2021;41:102854. http://dx.doi.org/10.1016/j.est.2021.102854.

[22] Wang N, Chen A, Zhao W, Zhu R, Duan B. An online temperature estimation for cylindrical lithium-ion batteries based on simplified distribution electrical-thermal model. J Energy Storage 2022;55:105326. http://dx.doi.org/10.1016/j.est.2022.105326.

[23] Dai H, Zhu L, Zhu J, Wei X, Sun Z. Adaptive Kalman filtering based internal temperature estimation with an equivalent electrical network thermal model for hard-cased batteries. J Power Sources 2015;293:351–65. http://dx.doi.org/10.1016/j.jpowsour.2015.05.087.

[24] Chen L, Hu M, Cao K, Li S, Su Z, Jin G, Fu C. Core temperature estimation based on electro-thermal model of lithium-ion batteries. Int J Energy Res 2020;44(7):5320–33. http://dx.doi.org/10.1002/er.5281.

[25] Rodríguez-Iturriaga P, del Valle JA, Rodríguez-Bolívar S, Anseán D, Viera JC, López-Villanueva JA. A novel dual fractional-order extended Kalman filter for the improved estimation of battery state of charge. J Energy Storage 2022;56:105810. http://dx.doi.org/10.1016/j.est.2022.105810.

[26] Rodríguez-Iturriaga P, Anseán D, López-Villanueva JA, González M, Rodríguez-Bolívar S. A method for the lifetime sensorless estimation of surface and core temperature in lithium-ion batteries via online updating of electrical parameters. J Energy Storage 2023;58:106260. http://dx.doi.org/10.1016/j.est.2022.106260.

[27] Shen J, Xiong J, Shu X, Li G, Zhang Y, Chen Z, Liu Y. State of charge estimation framework for lithium-ion batteries based on square root cubature Kalman filter under wide operation temperature range. Int J Energy Res 2021;45(4):5586–601. http://dx.doi.org/10.1002/er.6186.

[28] Wang P, Yang L, Wang H, Tartakovsky D, Onori S. Temperature estimation from current and voltage measurements in lithium-ion battery systems. J Energy Storage 2021;34:102133. http://dx.doi.org/10.1016/j.est.2020.102133.

[29] Liu M, Zhou X, Yang L, Ju X. A novel Kalman-filter-based battery internal temperature estimation method based on an enhanced electro-thermal coupling model. J Energy Storage 2023;71:108241. http://dx.doi.org/10.1016/j.est.2023.108241.

[30] Gao Y, Zhu C, Zhang X, Guo B. Implementation and evaluation of a practical electrochemical- thermal model of lithium-ion batteries for EV battery management system. Energy 2021;221:119688. http://dx.doi.org/10.1016/j.energy.2020.119688.

[31] Rodríguez-Iturriaga P, Anseán D, Rodríguez-Bolívar S, González M, Viera JC, López-Villanueva JA. A physics-based fractional-order equivalent circuit model for time and frequency-domain applications in lithium-ion batteries. J Energy Storage 2023;64:107150. http://dx.doi.org/10.1016/j.est.2023.107150.

[32] Bernardi D, Pawlikowski E, Newman J. A general energy balance for battery systems. J Electrochem Soc 1985;132(1):5–12. http://dx.doi.org/10.1149/1.2113792.

[33] Chen Q, Zhang X, Nie P, Zhang S, Wei G, Sun H. A fast thermal simulation and dynamic feedback control framework for lithium-ion batteries. Appl Energy 2023;350:121739. http://dx.doi.org/10.1016/j.apenergy.2023.121739.

[34] Zhang X, Wang Y, Chen Z. Soc-modified core temperature estimation of lithium-ion battery based on control-oriented electro-thermal model. IEEE Trans Power Electron 2023;38(9):11642–51. http://dx.doi.org/10.1109/TPEL.2023.3288539.

[35] Birkl CR, McTurk E, Roberts MR, Bruce PG, Howey DA. A parametric open circuit voltage model for lithium ion batteries. J Electrochem Soc 2015;162(12):A2271–80. http://dx.doi.org/10.1149/2.0331512jes.

[36] Li C, Cui N, Cui Z, Wang C, Zhang C. Novel equivalent circuit model for high-energy lithium-ion batteries considering the effect of nonlinear solid-phase diffusion. J Power Sources 2022;523:230993. http://dx.doi.org/10.1016/j.jpowsour.2022.230993.

[37] Zhuo M, Kirkaldy N, Maull T, Engstrom T, Offer G, Marinescu M. Diffusion-aware voltage source: An equivalent circuit network to resolve lithium concentration gradients in active particles. Appl Energy 2023;339:121004. http://dx.doi.org/10.1016/j.apenergy.2023.121004.

[38] Tran M-K, DaCosta A, Mevawalla A, Panchal S, Fowler M. Comparative study of equivalent circuit models performance in four common lithium-ion batteries: LFP, NMC, LMO, NCA. Batteries 2021;7(3). http://dx.doi.org/10.3390/batteries7030051.

[39] Thomas KE, Newman J. Heats of mixing and of entropy in porous insertion electrodes. J Power Sources 2003;119–121:844–9. http://dx.doi.org/10.1016/S0378-7753(03)00283-0, Selected papers presented at the 11th International Meeting on Lithium Batteries.

[40] Chalise D, Lu W, Srinivasan V, Prasher R. Heat of mixing during fast charge/discharge of a Li-Ion cell: A study on NMC523 cathode. J Electrochem Soc 2020;167(9):090560. http://dx.doi.org/10.1149/1945-7111/abaf71.

[41] Thomas KE, Newman J. Thermal modeling of porous insertion electrodes. J Electrochem Soc 2003;150(2). http://dx.doi.org/10.1149/1.1531194.

[42] Zeng Y, Chalise D, Lubner SD, Kaur S, Prasher RS. A review of thermal physics and management inside lithium-ion batteries for high energy density and fast charging. Energy Storage Mater 2021;41:264–88. http://dx.doi.org/10.1016/j.ensm.2021.06.008.

[43] Pang H, Jin J, Wu L, Zhang F, Liu K. A Comprehensive Physics-Based Equivalent-Circuit Model and State of Charge Estimation for Lithium-Ion Batteries. J Electrochem Soc 2021;168(9):090552. http://dx.doi.org/10.1149/1945-7111/ac2701.

[44] Biju N, Fang H. BattX: An equivalent circuit model for lithium-ion batteries over broad current ranges. Appl Energy 2023;339:120905. http://dx.doi.org/10.1016/j.apenergy.2023.120905.

[45] Li Y, Karunathilake D, Vilathgamuwa DM, Mishra Y, Farrell TW, Choi SS, Zou C. Model order reduction techniques for physics-based lithium-ion battery management: A survey. IEEE Ind Electron Mag 2022;16(3):36–51. http://dx.doi.org/10.1109/MIE.2021.3100318.

[46] Rodríguez-Iturriaga P, Anseán D, Rodríguez-Bolívar S, García VM, González M, López-Villanueva JA. Modeling current-rate effects in lithium-ion batteries based on a distributed, multi-particle equivalent circuit model. Appl Energy 2024;353:122141. http://dx.doi.org/10.1016/j.apenergy.2023.122141.

[47] Li Y, Vilathgamuwa M, Farrell T, Choi SS, Tran NT, Teague J. A physics-based distributed-parameter equivalent circuit model for lithium-ion batteries. Electrochim Acta 2019;299:451–69. http://dx.doi.org/10.1016/j.electacta.2018.12.167.

[48] Khayamy M, Nasiri A, Okoye O. Development of an equivalent circuit for batteries based on a distributed impedance network. IEEE Trans Veh Technol 2020;69(6):6119–28. http://dx.doi.org/10.1109/TVT.2020.2989715.

[49] Liu Y, Zhang C, Jiang J, Zhang L, Zhang W, Lao L, Yang S. A 3D distributed circuit-electrochemical model for the inner inhomogeneity of lithium-ion battery. Appl Energy 2023;331:120390. http://dx.doi.org/10.1016/j.apenergy.2022.120390.

[50] Roeder F, Sonntag S, Schroeder D, Krewer U. Simulating the impact of particle size distribution on the performance of graphite electrodes in lithium-ion batteries. Energy Technol 2016;4(12):1588–97. http://dx.doi.org/10.1002/ente.201600232.

[51] Xiao M, Choe S-Y. Theoretical and experimental analysis of heat generations of a pouch type LiMn2O4/carbon high power Li-polymer battery. J Power Sources 2013;241:46–55. http://dx.doi.org/10.1016/j.jpowsour.2013.04.062.

[52] Kirk TL, Please CP, Jon Chapman S. Physical modelling of the slow voltage relaxation phenomenon in lithium-ion batteries. J Electrochem Soc 2021;168(6). http://dx.doi.org/10.1149/1945-7111/ac0bf7.

[53] Paul T, Chi PW, Wu PM, Wu MK. Computation of distribution of relaxation times by Tikhonov regularization for li ion batteries: Usage of L-curve method. Sci Rep 2021;11(1). http://dx.doi.org/10.1038/s41598-021-91871-3.

[54] Bard AJ, Faulkner LR. Electrochemical Methods and Applications. Wiley-Interscience; 2000.

[55] Wycisk D, Mertin GK, Oldenburger M, Latz A. Analysis of heat generation due to open-circuit voltage hysteresis in lithium-ion cells. J Energy Storage 2023;61:106817. http://dx.doi.org/10.1016/j.est.2023.106817.

[56] Bernardi DM, Go J-Y. Analysis of pulse and relaxation behavior in lithium-ion batteries. J Power Sources 2011;196(1):412–27. http://dx.doi.org/10.1016/j.jpowsour.2010.06.107.

[57] Hu X, Liu W, Lin X, Xie Y. A comparative study of control-oriented thermal models for cylindrical Li-Ion batteries. IEEE Trans Transp Electrif 2019;5(4):1237–53. http://dx.doi.org/10.1109/TTE.2019.2953606.

[58] Lagnoni M, Nicolella C, Bertei A. Survey and sensitivity analysis of critical parameters in lithium-ion battery thermo-electrochemical modeling. Electrochim Acta 2021;394:139098. http://dx.doi.org/10.1016/j.electacta.2021.139098.

[59] Sturm J, Rheinfeld A, Zilberman I, Spingler F, Kosch S, Frie F, Jossen A. Modeling and simulation of inhomogeneities in a 18650 nickel-rich, silicon-graphite lithium-ion cell during fast charging. J Power Sources 2019;412:204–23. http://dx.doi.org/10.1016/j.jpowsour.2018.11.043.

[60] Wang C, Li C, Wang G, Zhang C, Cui N. Fast identification method for thermal model parameters of Lithium-ion battery based on discharge temperature rise. J Energy Storage 2021;44:103362. http://dx.doi.org/10.1016/j.est.2021.103362.

[61] Yan H, Marr KC, Ezekoye OA. Thermal runaway behavior of nickel–manganese–cobalt 18650 lithium-ion cells induced by internal and external heating failures. J Energy Storage 2022;45:103640. http://dx.doi.org/10.1016/j.est.2021.103640.

[62] Sheng L, Zhang Z, Su L, Zhang H, Zhang H, Fang Y, Li K, Ye W. Quasi steady state method to measure thermophysical parameters of cylindrical lithium ion batteries. J Power Sources 2021;485:229342. http://dx.doi.org/10.1016/j.jpowsour.2020.229342.

[63] Kim Y, Siegel JB, Stefanopoulou AG. A computationally efficient thermal model of cylindrical battery cells for the estimation of radially distributed temperatures. In: 2013 American control conference. 2013, p. 698–703. http://dx.doi.org/10.1109/ACC.2013.6579917.

[64] Yan H, Ezekoye OA. State of charge effects on active material elemental composition changes between pre-thermal-runaway and post-failure states for 8-1-1 nickel-manganese-cobalt 18650 cells. J Energy Storage 2023;63:106974. http://dx.doi.org/10.1016/j.est.2023.106974.

[65] Christophersen JP. Battery test manual for electric vehicles, revision 3. Tech. rep., 2015, http://dx.doi.org/10.2172/1186745.

[66] Oldenburger M, Bedürftig B, Richter E, Findeisen R, Hintennach A, Gruhle A. Analysis of low frequency impedance hysteresis of Li-Ion cells by time- and frequency domain measurements and its relation to the OCV hysteresis. J Energy Storage 2019;26:101000. http://dx.doi.org/10.1016/j.est.2019.101000.

[67] Meddings N, Heinrich M, Overney F, Lee JS, Ruiz V, Napolitano E, Seitz S, Hinds G, Raccichini R, Gaberšček M, Park J. Application of electrochemical impedance spectroscopy to commercial Li-Ion cells: A review. J Power Sources 2020;480(May). http://dx.doi.org/10.1016/j.jpowsour.2020.228742.

[68] Fernández Pulido Y, Blanco C, Anseán D, García VM, Ferrero F, Valledor M. Determination of suitable parameters for battery analysis by Electrochemical Impedance Spectroscopy. Measurement 2017;106:1–11. http://dx.doi.org/10.1016/j.measurement.2017.04.022.

[69] Yang B, Wang D, Sun X, Chen S, Wang X. Offline order recognition for state estimation of Lithium-ion battery using fractional order model. Appl Energy 2023;341:120977. http://dx.doi.org/10.1016/j.apenergy.2023.120977.

[70] Mertin GK, Wycisk D, Richter E, Oldenburger M, Hofmann MH, Luetje TH, Manz M, Luu H, Wieck AD, Birke KP. Interpreting the entropy of silicon–graphite blended electrodes. J Energy Storage 2023;64:107118. http://dx.doi.org/10.1016/j.est.2023.107118.

[71] Bazinski S, Wang X. Determining entropic coefficient of the LFP prismatic cell at various temperatures and charge/discharge states. ECS Trans 2013;45(29):85–92. http://dx.doi.org/10.1149/04529.0085ecst.

[72] Jalkanen K, Aho T, Vuorilehto K. Entropy change effects on the thermal behavior of a LiFePO4/graphite lithium-ion cell at different states of charge. J Power Sources 2013;243:354–60. http://dx.doi.org/10.1016/j.jpowsour.2013.05.199.

[73] Geng Z, Groot J, Thiringer T. A time- and cost-effective method for entropic coefficient determination of a large commercial battery cell. IEEE Trans Transp Electrif 2020;6(1):257–66. http://dx.doi.org/10.1109/TTE.2020.2971454.

[74] Eddahech A, Briat O, Vinassa J-M. Thermal characterization of a high-power lithium-ion battery: Potentiometric and calorimetric measurement of entropy changes. Energy 2013;61:432–9. http://dx.doi.org/10.1016/j.energy.2013.09.028.

[75] Faber M, Buitkamp O, Ritz S, Börner M, Berger J, Friedrich J, Arzberger A, Sauer DU. A method to determine the specific heat capacity of lithium-ion battery cells using thermal insulation. J Power Sources 2023;583:233499. http://dx.doi.org/10.1016/j.jpowsour.2023.233499.

[76] Xie Y, Fan Y, Yang R, Zhang K, Chen B, Panchal S, Zhang Y. Influence of uncertainty of thermal conductivity on prediction accuracy of thermal model of lithium-ion battery. IEEE Trans Transp Electrif 2024;1. http://dx.doi.org/10.1109/TTE.2024.3352663.